Composites Part B 242 (2022) 110102

Contents lists available at ScienceDirect

Composites Part B

journal homepage: www.elsevier.com/locate/compositesb

Elevated shock resistance of all-metallic sandwich beams with honeycomb-supported corrugated cores

Zengshen Yue [a,b,1], Xin Wang [a,c,1], Chao He [b,d], Runpei Yu [a], Xue Li [b,d], Zhenyu Zhao [b,d], Qiancheng Zhang [a,*], Tian Jian Lu [b,d,**]

[a] State Key Laboratory for Strength and Vibration of Mechanical Structures, Xi'an Jiaotong University, Xi'an, 710049, PR China
[b] State Key Laboratory of Mechanics and Control of Mechanical Structures, Nanjing University of Aeronautics and Astronautics, Nanjing, 210016, PR China
[c] Impact Mechanics Laboratory, National University of Singapore, Singapore, 117576, Singapore
[d] MIIT Key Laboratory of Multifunctional Lightweight Materials and Structures, Nanjing University of Aeronautics and Astronautics, Nanjing, 210016, PR China

ARTICLE INFO

Keywords:
Sandwich beam
Honeycomb-corrugation hybrid core
Shock resistance
Foam projectile
Enhancement mechanism

ABSTRACT

Sandwich structures with cellular cores are favored in shock resistance, due mainly to advantages in fluid-structure interaction, energy absorption via core compression, and overall bending strength. To further enhance the shock resistance, this study proposes lightweight sandwich beams with honeycomb-supported corrugated cores. Firstly, dynamic responses of fully-clamped sandwich beams with such honeycomb-corrugation hybrid cores, including deformation/failure modes and beam deflections, were experimentally measured under simulated shock loading via foam projectile impact, and were compared with those of corresponding corrugated sandwich beams without honeycomb insertions. Secondly, the finite elements (FE) method was used to simulate the shock experiment. FE simulation results were validated against experimental measurements, with good agreement achieved. Subsequently, the FE model was employed to explore further how impact velocity, relative density of honeycomb, and honeycomb orientation in hybrid core affect beam deflection, and to reveal the underlying physical mechanisms. It was demonstrated that combining honeycombs with folded plates (corrugations) to create a hybrid core for sandwich construction led to significant enhancement in shock resistance, especially at relatively low projectile momentum where more than 50% enhancement could be achieved. Such superiority of the hybrid-cored sandwich beam was mainly attributed to its high specific compressive/shear strength as a result of the beneficial interaction effect between honeycomb insertions and folded plates, thus enabling smaller core crushing/deformation and higher bending strength of the impulsively loaded sandwich beam. At sufficiently high impact momentum, however, the interaction effect vanished as deformation of the fully-clamped sandwich beam is now dominated by stretching rather than bending.

1. Introduction

When subjected to shock loadings, lightweight sandwich structures with highly porous cellular cores typically experience a complex series of deformation processes that have been simplified and decoupled into three stages: fluid-structure interaction, core deformation, overall bending and stretching [1]. Compared with monolithic beams or plates of equal mass, sandwich constructions obtain less momentum (as a result of fluid-structure interaction), can rely on the cores to absorb energy, and have greater bending strength, thus are considered excellent anti-shock protection structures [2–4]. With increasingly harsh threats of extreme dynamic impact and blast loads, further improving the impact/shock resistance of sandwich structures becomes a pressing necessity. In practice, for a sandwich protective construction, its structure size (especially the thickness) and face sheet form are often limited, but the high porosity cellular core itself brings a lot of design space, and hence hybrid core design has in recent years been envisioned as one of efficient enhancement methodologies [5–8].

* Corresponding author. State Key Laboratory for Strength and Vibration of Mechanical Structures, Xi'an Jiaotong University, Xi'an, 710049, PR China.
** Corresponding author. State Key Laboratory of Mechanics and Control of Mechanical Structures, Nanjing University of Aeronautics and Astronautics, Nanjing, 210016, PR China.
E-mail addresses: yuezengshen@163.com (Z. Yue), wxtj_9449@163.com (X. Wang), zqc111999@mail.xjtu.edu.cn (Q. Zhang), tjlu@nuaa.edu.cn (T.J. Lu).
[1] The authors contributed equally to this paper.

https://doi.org/10.1016/j.compositesb.2022.110102
Received 12 February 2022; Received in revised form 26 June 2022; Accepted 29 June 2022
Available online 2 July 2022
1359-8368/© 2022 Elsevier Ltd. All rights reserved.

Specifically, to construct a hybrid sandwich core, one or more advanced materials, either monolithic or porous, are inserted or in-situ synthesized in the abundant space of a two-dimensional (2D) prismatic or three-dimensional (3D) lattice truss core. Such design concepts often enable creating hybrid structures with superior mechanical properties (e.g., stiffness, strength and energy absorption), due to the strong performance coupling between the insertions and the original core members [9,10], and even multi-functional performances (e.g., sound absorption with micro-perforations on face sheet and core members [11], active cooling with fluid-through core channel [12], and penetration resistance with concrete/ceramic insertions [13,14]). Compared with the traditional methods of developing new metal alloys, new polymer chemistries, and so on, which are usually expensive and uncertain processes, creating novel hybrid sandwich cores on the basis of existing cellular cores is deemed more economical and controllable.

Existing hybrid sandwich cores constructed on the basis of 2D or 3D lattice structures could be macroscopically classified into three main types: disordered-disordered hybrid (e.g., fiber-foam hybrid [15]), disordered-ordered hybrid (e.g., foam-filled corrugations [9], foam-reinforced multi-walled tubes [16]), ordered-ordered hybrid (e.g., honeycomb-corrugation hybrid [10,17], hybrid modified body-centered cubic lattices [18]). Particularly, the design of hybrid sandwich core for enhanced impact/shock resistance has been largely conducted based on the all-metallic corrugated sandwich structures which, with high collapse resistance and high longitudinal stretching/shear strength [19], have been exploited in a wide range of applications [20,21]. Two major design strategies have hitherto been envisioned: permanent constructions filled with ultralight materials (e.g., polymer or metallic foams [5,6]) for enhanced energy absorption of the core; temporary constructions filled with heavy unconfined materials (e.g., water [7] and sand particles [8]) for hard compression and inertia effect of the core. However, for the former, the enhancement effect was found to be not obvious, for the reduction in mid-span deflection of fully-clamped sandwich beam subjected to impulsive loading was ~17% while the mass increase due to insertion was ~11% [5]. As for the latter, although the reduction in deflection was further improved, the mass of the sandwich structure as a whole was also greatly increased; in addition, a temporary filling is often not appropriate or convenient for mobile constructions (e.g., vehicles and ships). Thus, there is an urgent need for more effective hybrid cores to enhance the shock/impact resistance of sandwich structures at minimal penalty of structural mass.

Upon impact loading, the core of a sandwich structure experiences various stresses and deformations, such as compression, shearing, stretching, and so on [7,22]. Thus, a hybrid core with combined mechanical properties may be required to withstand such stressing and deformation. Among the numerous conventional and hybrid metallic cellular cores, the novel honeycomb-corrugation core has become a rising star. Firstly, such a hybrid core could be constructed by filling honeycomb blocks into corrugations (i.e., folded plates; Fig. 1a), which is relatively easy to fabricate. Secondly, it exhibits excellent combined mechanical properties as well as a variety of multifunctional attributes. Figures 1b–d displays the mechanical property charts for a wide range of all-metallic 2D prismatic and 3D lattice truss cores, with quasi-static test data taken from existing literature. It is seen that, in the low to medium density regime, critical for many engineering applications (e.g., automobiles, high-speed trains, ships, aeroplanes and satellites), the honeycomb-corrugation core exhibits outstanding out-of-plane compressive strength, longitudinal shear strength, and out-of-plane compressive energy absorption capability. Additionally, a sandwich beam with honeycomb-corrugation core also exhibits enhanced bending performance than that having either of its parent cellular cores, i.e., corrugations and honeycombs [23]. Further, in terms of multi-functional applications, it has been demonstrated that a sandwich panel with honeycomb-corrugation core possesses considerable vibration performance [24] as well as broadband sound absorption upon periodically placing micro-perforations on its face sheet and corrugated plates [11].

As introduced above, the honeycomb-corrugation hybrid core exhibits excellent combined quasi-static mechanical properties accompanied by superior multifunctional attributes, which are all achieved in

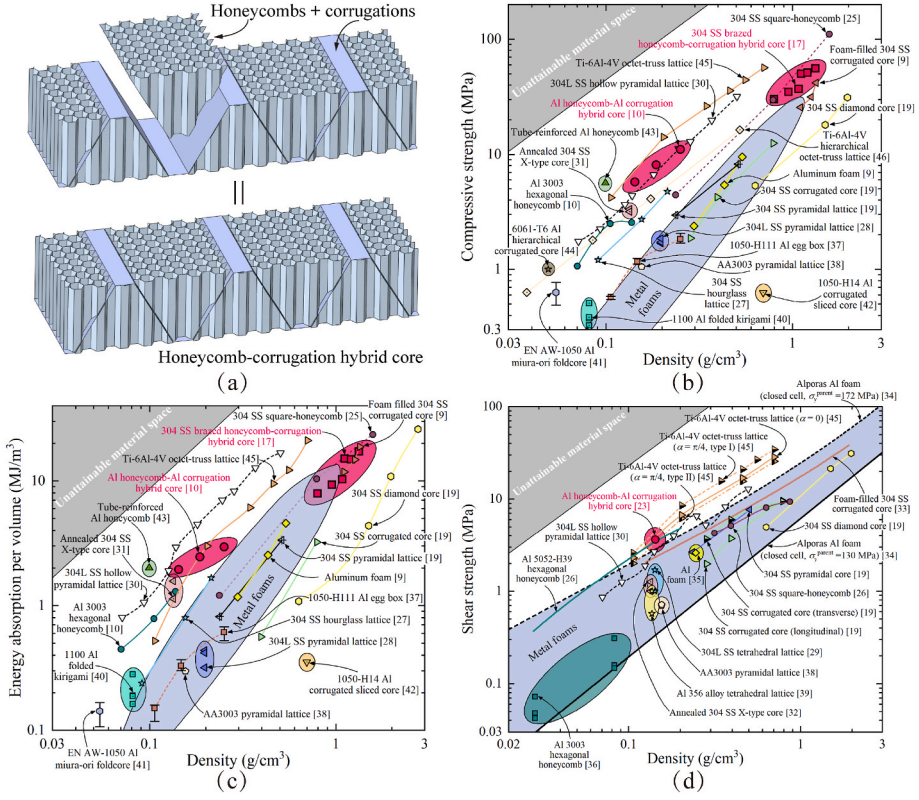

Fig. 1. (a) Sketch of honeycomb-corrugation hybrid core; mechanical property charts comparing (b) out-of-plane compressive strength, (c) out-of-plane compressive energy absorption per volume, and (d) longitudinal shear strength against density for a wide range of all-metallic, two-dimensional prismatic and three-dimensional lattice truss cores: 304 stainless steel (SS) square-honeycomb [25,26], 304 SS corrugated core [19], 304 SS diamond core [19], 304 SS pyramidal lattice [19], 304 SS hourglass lattice [27], 304L SS pyramidal core [28], 304L SS tetrahedral lattice [29], 304L SS hollow pyramidal lattice [30], annealed 304 SS X-type core [31,32], foam-filled 304 SS corrugated core [9,33], 304 SS brazed honeycomb-corrugation hybrid core [17], aluminum (Al) foam [9,34,35], Al 3003 hexagonal honeycomb [10,36], Al 5052-H39 hexagonal honeycomb [26], 1050-H111 Al egg box [37], AA3003 pyramidal lattice [38], Al 356 alloy tetrahedral lattice [39], 1100 Al folded kirigami [40], EN AW-1050 Al miura-ori foldcore [41], 1050-H14 Al corrugated sliced core [42], tube-reinforced Al honeycomb [43], 6061-T6 Al hierarchical corrugated core [44], Al honeycomb-Al corrugation hybrid core [10,23], Ti–6Al–4V octet-truss lattice [45], Ti–6Al–4V hierarchical octet-truss lattice [46].

low mass and small volume. Therefore, we believe that it will also perform as an ideal shock resister. However, at present, how a honeycomb-corrugation sandwich construction would behave under shock loading remains unclear. Thereupon, the present study aims to characterize the dynamic responses of all-metallic honeycomb-corrugation hybrid sandwich beams subjected to shock loading. A combined experimental, numerical and analytical approach is adopted. Excessive improvement of its dynamic resistance over percentage increase in mass is expected. The main influencing factors are revealed and the enhancement mechanisms are analyzed in detail.

2. Foam projectile impact experiments

2.1. Materials and specimen

All-metallic hybrid-cored sandwich beam specimens comprising a hexagonal honeycomb-trapezoidal corrugation core and two identical face sheets are fabricated. Geometric configuration of the specimens (hybrid sandwich beams) is displayed in Fig. 2, together with end block fixtures for clamping. Relevant geometric parameters include: length L, width W, and total height H of sandwich beam; face sheet thickness t_f, core height h_c; thickness t_c, inclined strut length l_c, inclination angle α, and platform segment width l_p of corrugation members; thickness t_h and cell wall length l_h of honeycomb members; metal block length L_b, and bolt hole diameter d_b. The empty corrugated core has a relative density given by:

$$\overline{\rho}_c = \frac{t_c(l_p + l_c)}{(l_p + l_c\cos\alpha)(t_c + l_c\sin\alpha)}, \tag{1}$$

while the relative density of honeycombs is:

$$\overline{\rho}_h = \frac{8t_h}{3(\sqrt{3}\,l_h + 2t_h)} \cong \frac{8t_h}{3\sqrt{3}l_h}. \tag{2}$$

The relative density $\overline{\rho}$ of honeycomb–corrugation hybrid is:

$$\overline{\rho} = \overline{\rho}_c + \overline{\rho}_h(1 - \overline{\rho}_c). \tag{3}$$

The honeycombs are made of aluminum, the face sheets and the corrugations are made of stainless steel (AISI 304), while the end block fixtures are made of low carbon steel. Empty (unfilled) corrugated sandwich beams are fabricated using common stamping, assembling, and vacuum brazing processes [7,8]. Trapezoidal honeycomb blocks are cut from original honeycombs acquired from Weixin Technology Co., Ltd. (Xi'an, China) via the EDM wire cutting technology. The trapezoidal honeycomb blocks are then filled into the interstices of corrugations and glued using aviation-grade epoxy adhesive LOCTITE® EA E−120HP for 36 h at room temperature. Detailed geometric parameters of as-built test samples are summarized in Table 1.

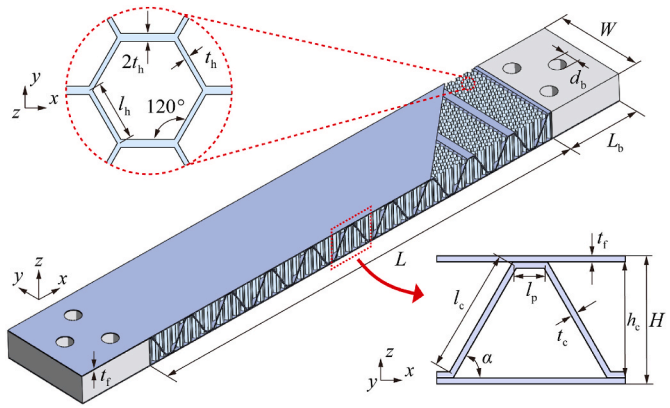

Fig. 2. Honeycomb-corrugation sandwich beam specimen.

Table 1
Geometric parameters of honeycomb-corrugation hybrid sandwich beam samples.

Empty corrugated steel core					
l_c (mm)	l_p (mm)	t_c (mm)	α (°)	h_c (mm)	$\overline{\rho}_c$
20	5	0.5	60	17.82	4.68%
Aluminum honeycomb					
	l_h (mm)		t_h (mm)		$\overline{\rho}_h$
	2		0.05		3.74%
Geometric parameters					
L (mm)	W (mm)	t_f (mm)	L_b (mm)	d_b (mm)	$\overline{\rho}$
300	60	0.5	50	10	8.24%

While the face sheets and corrugated cores of sandwich beams are both manufactured from AISI 304 stainless steel, standard dog-bone tensile specimens are cut from as-received steel sheets and then subjected to the same heating and cooling cycle for furnace brazing as sandwich beams. Subsequently, to determine the mechanical properties of annealed AISI 304 stainless steel, quasi-static uniaxial tensile test at nominal strain rate of 3.3×10^{-3} s^{-1} is conducted on an MTS machine, in accordance with the ISO standard 6892–1:2009. Three nominally identical specimens are tested to determine the average true stress versus true strain curve, as shown in Fig. 3a. The AISI 304 stainless steel could be regarded as an elastic, linearly hardening material, with density $\rho_s = 7800$ kg/m^3, Young's modulus $E = 210$GPa, yield strength $\sigma_Y = 200$MPa, and tangent modulus $E_t = 2$GPa.

It has been demonstrated that cylindrical impact projectiles made from closed-cell aluminum (Al) foam can be used to simulate shock loading at laboratory scale [47]. This technique is adopted in the present study. Based on the cylindrical foam specimen (diameter 57 mm and height 85 mm), quasi-static compressive test of the Al foam (density $\rho_p = 364.09$ kg/m^3) is conducted at a nominal strain rate of 1×10^{-3} s^{-1} on the MTS machine. The measured engineering stress versus engineering strain curve is presented in Fig. 3b, showing that the plateau strength of the foam was $\sigma_c = 4.53$MPa. To identify the nominal densification strain of the foam, the energy absorption efficiency is defined as follows:

$$\chi(\varepsilon_n) = \frac{1}{\sigma_n(\varepsilon_n)}\int_0^{\varepsilon_n}\sigma_n(\varepsilon_n)\mathrm{d}\varepsilon_n. \tag{4}$$

The nominal densification strain is thence obtained by:

$$\left.\frac{\mathrm{d}\chi(\varepsilon_n)}{\mathrm{d}\varepsilon_n}\right|_{\varepsilon_n=\varepsilon_D} = 0. \tag{5}$$

For the Al foam employed in the present study, the nominal densification strain $\varepsilon_D = 0.55$; Fig. 3b.

As foam density plays a great role in dictating the mechanical properties of cellular metallic foams, foam projectiles are selected such that the deviation of density is strictly lower than 5% for impact experiments. Therefore, any difference between foam projectiles is ignored, and the measured compressive response of the foam is employed as input for subsequent numerical simulations.

2.2. Experimental protocol

The experimental setup of foam projectile impact tests is presented in Fig. 4. It includes a one-stage light gas gun to fire the projectiles, a pair of fixtures to clamp sandwich beams, and a high-speed camera to image the impact events and measure projectile velocities. Nitrogen gas at a prescribed pressure in the gas chamber is employed to launch aluminum foam projectiles from the gas gun (barrel length 5 m, inner diameter 57 mm, and outer diameter 135 mm). The fixtures are used to guarantee fixed support boundary conditions by clamping a sandwich specimen at its two supporting edges: a total of six M10 bolts are configurated on the

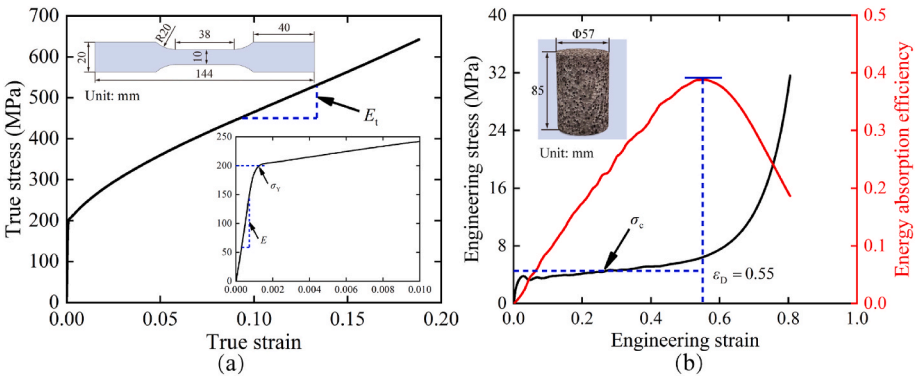

Fig. 3. Measured quasi-static stress versus strain responses of constituent materials: (a) uniaxial tensile true stress versus true strain curve of AISI 304 stainless steel; (b) compressive engineering stress versus engineering strain curve of aluminum foam.

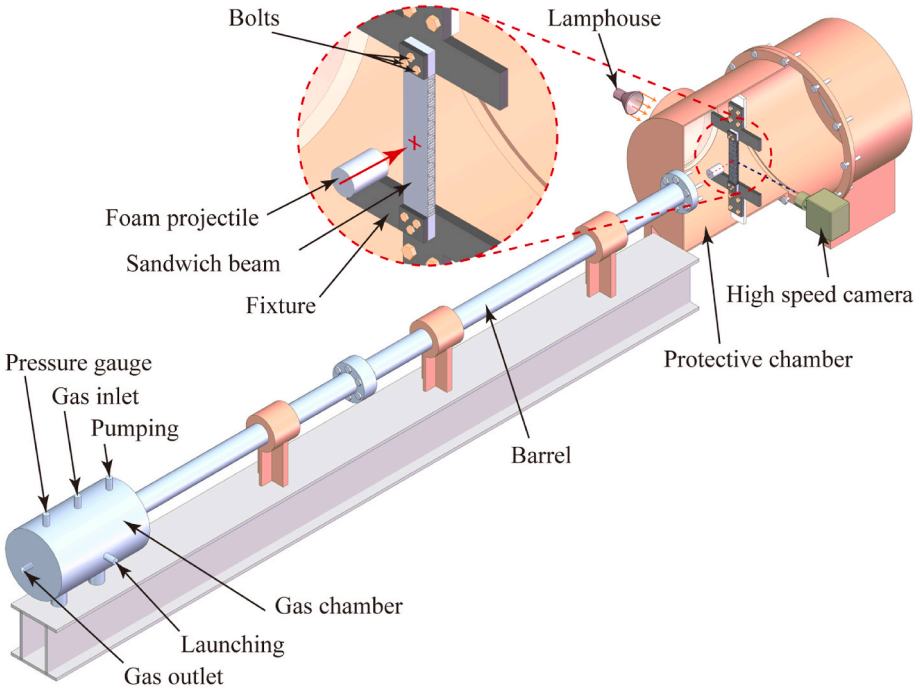

Fig. 4. Schematic of impact test setup for measuring dynamic response of clamped beam impacted by foam projectile.

fixtures, with three bolts located on each side. High-speed camera (I-SPEED 716, IX) is used to observe the dynamic structural evolution of sandwich beams, with the frame rate and exposure time fixed at 20000 fps and 1 μs, respectively. Meanwhile, two photographs before the foam projectile impacts the beam are extracted to measure its initial impact velocity v_0. The travel distance between the two photographs is obtained via digital image processing, and the initial impact velocity is then calculated by dividing the travel distance by interval time between the two photographs.

The foam projectiles are fabricated through wire-cut electrical discharge machining from an aluminum foam block. To prevent tumbling, the length to diameter ratio of the projectile should fall within the range of 0.82–1.75 [7]. Moreover, the loading area should be slightly smaller than the width of the sandwich beam to avoid different responses of the core across the direction of its width [2]. Therefore, in the present study, the foam projectiles have a length (l_0) of 85 mm, diameter (d_0) of 57 mm, and density (ρ_p) varying in the range of 360–370 kg/m^3. In the experiments, the projectiles are used to centrally impact the fully-clamped sandwich beams to simulate local shock loadings.

2.3. Experimental results

Table 2 summarizes the experimental results of impact tests conducted on both empty corrugated sandwich beams (EC) and honeycomb-corrugation hybrid sandwich beams (HC) for selected values of projectile momentum per unit area $I_0 = \rho_p l_0 v_0$. Note that, m_e and m_h represent the mass of empty corrugated sandwich beams and filled honeycombs, respectively; w_i and w_r represent the permanent mid-span deflection of impact and rear face sheets, respectively, and ε_c represents the permanent mid-span core compressive strain given by:

$$\varepsilon_c = \frac{w_i - w_r}{l_c \sin\alpha + t_c}. \tag{6}$$

Three levels of momentum I_0 are applied to both the EC and HC sandwich beams, as presented in Table 2. Since the use of pressure vessel to accelerate a foam projectile does not allow for precise control of its initial velocity, the momentum is not guaranteed to be completely uniform but guaranteed to fall within a very similar range.

Table 2
Impact experimental results of both empty corrugated sandwich beams (EC) and honeycomb-corrugation hybrid sandwich beams (HC).

Specimen	Structure description		Foam projectile			Impacting response		
	m_e(g)	m_h(g)	ρ_p(kg /m^3)	v_0(m /s)	I_0(kPa ·s)	w_i(mm)	w_r(mm)	ε_c
EC-1	1089.14	–	362.32	87.87	2.71	26.01	23.99	0.11
EC-2	1084.15	–	361.20	128.98	3.96	37.22	30.33	0.39
EC-3	1092.45	–	360.32	186.60	5.72	50.60	42.12	0.48
HC-1	1099.37	33.6	365.72	81.07	2.52	12.02	11.33	0.04
HC-2	1089.42	33.4	365.02	129.43	4.02	29.87	27.86	0.11
HC-3	1096.16	32.8	369.95	184.23	5.79	41.63	40.56	0.06

2.3.1. Evolution of dynamic deformation

Figures 5–7 display the evolutions of dynamic structural deformation for both empty and hybrid sandwich beams. The time labeled on each photograph sequence imaged by high-speed camera is measured from the instant of foam projectile impact.

As presented in Figs. 5a–7a, the overall structural responses of EC beams under three levels of initial momentum (EC-1, EC-2, and EC-3 for I_0 = 2.71,3.96, and 5.72kPa·s, respectively) are similar. When the foam projectile hits the mid-span of the impact face sheet of a beam, its impact face obtains an initial velocity and begins to deform, accompanied by momentum transfer between the projectile and impact face. Thereupon, the corrugated core is compressed at the impact location region in a buckling mode. As the momentum is transferred from impact face via the core to rear face, the velocity of impact face decreases while that of rear face increases. When the velocity of rear faces becomes identical to that of impact face, core compression is complete. Subsequently, two pairs of plastic hinges are motivated at the edge of the local impact region and then travel towards the supports and mid-span of beams, respectively. In this process, plastic hinges pass through some regions where the core begins to deform in shear. Specifically, plastic hinges arrive both the ends and mid-span point of beams at the time of 1.2 ms, 0.9 ms, and 0.8 ms for EC-1, EC-2, and EC-3, respectively. After that, the beam enters the stage of overall stretching. Note that the larger shear stress between the face sheets and core may lead to interfacial failure of brazing joints if the projectile momentum reaches a threshold, as shown in Fig. 7a.

Despite the overall similarity as discussed above for the EC beams, some differences exist due to different levels of initial momentum. When the impact and rear faces reach the same velocity, while the corrugated cores of EC-1 and EC-2 at the impact region are only partially compressed, the corrugated core of EC-3 at the impact region has been compressed to full densification. In addition, the dynamic deformation of EC-1 almost ceases when the traveling plastic hinges reach its supports ends and mid-span. In contrast, EC-2 and EC-3 are still deforming obviously in stretching after the motivation of plastic hinges. The shear stress between the corrugated core and face sheets does not cause interfacial failure of brazing joints of EC-1, whereas brazing joints failure occurs in both EC-2 and EC-3, with more failure points in EC-3 than EC-2.

For comparison, dynamic structural deformation evolutions of HC beams are displayed in Figs. 5b–7b. Similar to EC beams, when a foam projectile impacts an HC beam, its impact face begins to deform, and soon its core begins to compress. However, as the high specific strength of aluminum honeycomb blocks filled in corrugated channels enables high strength of the hybrid core, core crushing is typically insignificant in comparison with that of an EC beam, especially at relatively low momentum level (e.g., sample HC-1). As the initial momentum of foam projectile is increased, the degree of core compression of HC-2 and HC-3 remains insignificant, which is quite different from that observed in EC beams.

For HC beams, the propagation of plastic hinges is not obvious at relatively low momentum level (HC-1), and the whole deformation process looks like overall bending; Fig. 5b. This phenomenon may again be attributed to the high strength of the hybrid core and insignificant core crushing. In addition, the filling of honeycomb blocks significantly enhances the shear resistance of the core (more details given later) and hence the longitudinal shear deformation developed in empty corrugated cores is not observed in hybrid cores throughout the whole bending process. At a moderate momentum level (HC-2; Fig. 6b), the degree of core crushing in the HC beam remains small, but traveling plastic hinges similar to EC beams can already be observed. Note that, local interfacial failure between honeycomb blocks and corrugated

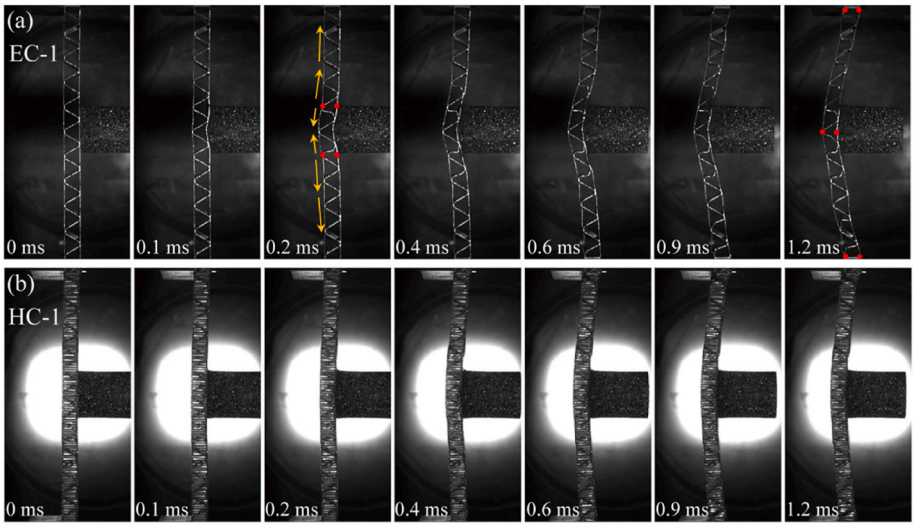

Fig. 5. Structural evolution of (a) empty corrugated sandwich beam (EC-1) of I_0 = 2.71 kPa·s, and (b) honeycomb-corrugation hybrid sandwich beam (HC-1) of I_0 = 2.52 kPa·s.

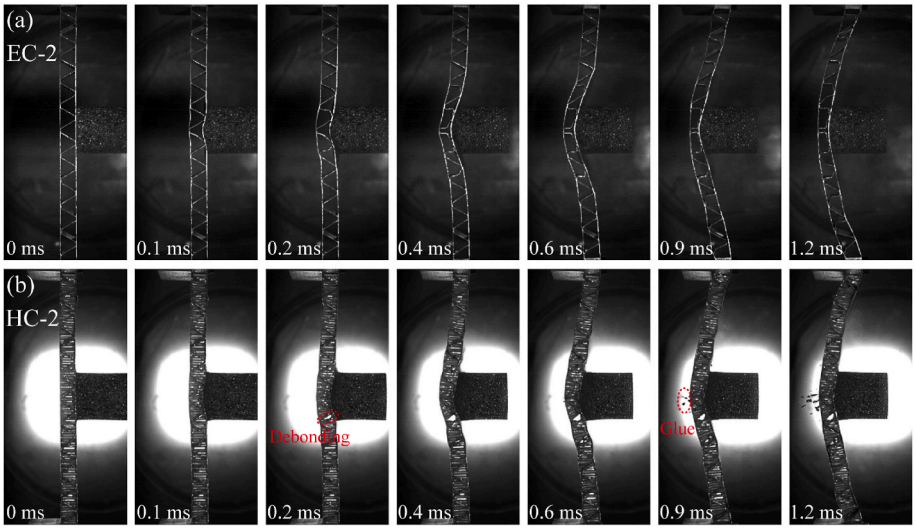

Fig. 6. Structural evolution of (a) empty corrugated sandwich beam (EC-2) of $I_0 = 3.96$ kPa·s, and (b) honeycomb-corrugation hybrid sandwich beam (HC-2) of $I_0 = 4.02$ kPa·s.

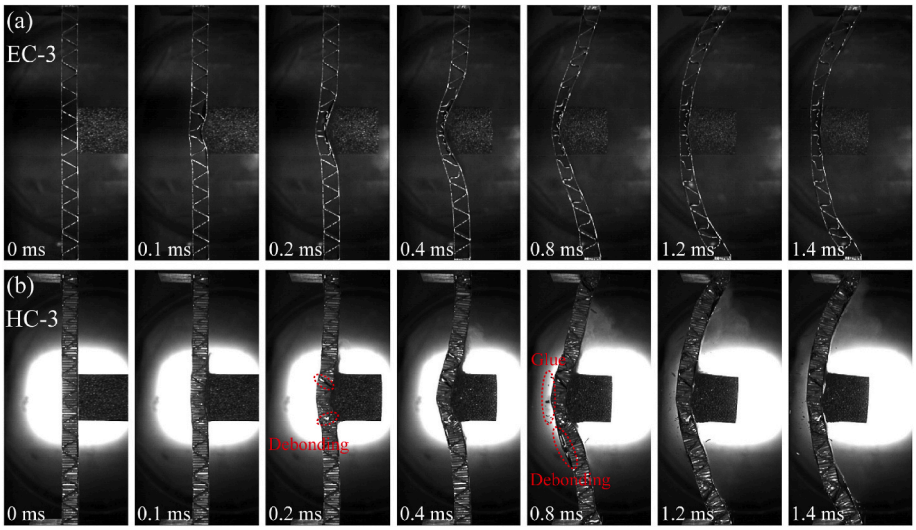

Fig. 7. Structural evolution of (a) empty corrugated sandwich beam (EC-3) of $I_0 = 5.72$ kPa·s, and (b) honeycomb-corrugation hybrid sandwich beam (HC-3) of $I_0 = 5.79$ kPa·s.

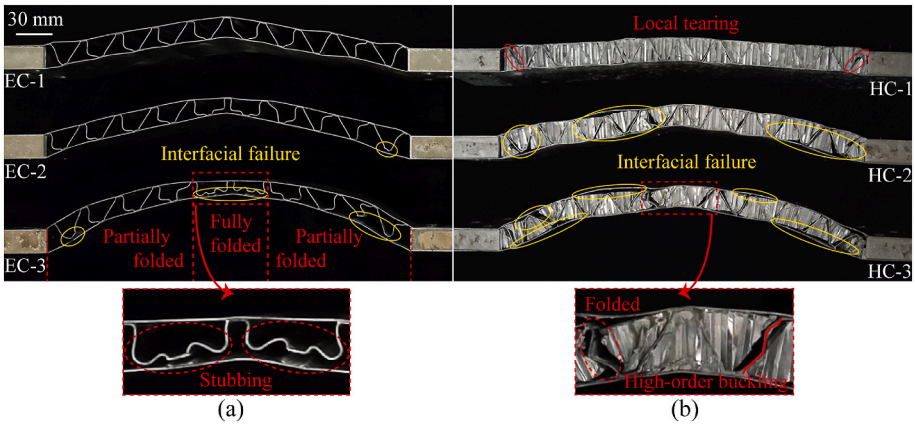

Fig. 8. Final deformation profiles of (a) empty corrugated core sandwich beams and (b) honeycomb-corrugation hybrid sandwich beams.

members occurs under the impact, mainly concentrated at the location of plastic hinges sprouting (i.e., the edges of projectile impact region). This may be induced by transverse shear action at the location of plastic hinges. Some debris of glue splashes out after local interfacial failure, as shown in Fig. 6b. At a higher momentum level (HC-3; Fig. 7b), there is a small increase in the degree of core crushing, while the plastic hinges propagation process is more pronounced. Again, local interfacial failure between honeycomb blocks and corrugated members occurs. Except for the location of plastic hinges sprouting, the interfacial failure also extends towards plastic hinge propagation directions as a result of longitudinal shear action at plastic hinges. Meanwhile, due to the high level of shear stresses, brazing joint failure also occurs as shown in Fig. 7b.

2.3.2. Deformation/failure modes

The final deformation and failure modes of EC beams are presented in Fig. 8a. The propagation of plastic hinges results in continuously curved profile of a beam, and significant core compression and shear over the entire span of the beam are also clearly captured. Four different deformation/failure modes exist: large inelastic deformation, core compression, core shear, and interfacial failure. For the face sheets, the dominant deformation mode is large inelastic deformation, mainly caused by dynamic bending and stretching [8]. However, no tearing or transverse shear failure of face sheets is observed within the momentum range of current study, consistent with a previous study [48]. The corrugated core within the region of impact location deforms mainly in compression. Moreover, for the empty corrugated cores, the main deformation mode gradually changes from compression to longitudinal shear from mid-span to supports. It is deduced that the fully-clamped boundary condition significantly influences the state of stress of beam span. At a lower level of momentum as in the case of EC-1, plastic bulking is observed as the main deformation mode in the core compression region. As the momentum is increased (EC-2 and EC-3), the deformation mode of compressive corrugated core changes from buckling to stubbing, similar to that reported by McShane et al. [49]. In addition, at a relatively high momentum level (EC-3), core deformation can be divided into a fully folded region and a partially folded region, respectively, with the former located at beam span and the latter at the sides. The corrugated core in the fully folded region is fully compacted, and hence its compressive strain can hardly change for more, as shown in the enlarged midspan view of EC-3 in Fig. 8a. Note that the interfacial failure between face sheets and core is closely related to the level of projectile momentum. With increasing momentum, the beam is subjected to greater shear stresses near the ends, so that interfacial failure occurs first near the supports (EC-2). Then, at the impacted region, interfacial failure occurs as well under higher projectile momentum (EC-3). Besides, brazing joints on impact faces are more prone to failure compared to that on rear faces, due mainly to the more significant stretching deformation of the impact face.

Figure 8b displays the final deformation profiles of HC beams. Similar to EC beams, large inelastic deformation is the dominant deformation mode of face sheets. However, some significant differences between the deformation extent and deformation modes persist. For a lower momentum level (HC-1), core crushing is barely visible and the deformation mode of HC-1 exhibits overall bending. At the ends of HC-1, a slight shear tear in the core can be observed, which is due to the transverse shear after plastic hinges arrive there. As the momentum increases as in the case of HC-2, slight core crushing begins to occur in the mid-span of the beam, while interfacial failure between honeycomb blocks and corrugated members occurs. The location is near the projectile impact boundary and ends of the beam, which is mainly attributed to the combined effect of transverse and longitudinal shear. At a higher momentum level (HC-3), the increase in the degree of core crushing at mid-span is still insignificant, but interfacial failure between honeycomb blocks and corrugated members is more pronounced due to higher shear stress. Meanwhile, obvious debonding occurs between the core and face sheets as well. As shown in the enlarged view of the core at mid-span of HC-3 in Fig. 8b, the deformation of the corrugated core produces high-order buckling due to the filling of honeycomb blocks, which provides strong support for the corrugated members against buckling. Note that, the overall deformation of an HC beam is less than that of EC beam, particularly so at lower momentum levels, which will be described in detail in the next section.

2.3.3. Quantitative results

The experimentally measured deflection profiles of rear and impact faces of both the EC and HC beams are displayed in Fig. 9. With the mid-span deflections of rear and impact faces of the EC beams taken as the benchmark, the reduction ratios of honeycomb filling on mid-span deflections are summarized in Table 3, where I-1, I-2, and I-3 correspond to the three initial momentum levels.

It can be seen that the rear and impact face deflections of HC beams are significantly smaller than those of EC beams at the same momentum level, which indicates that the filling of honeycomb blocks significantly enhances the shock resistance of corrugated sandwich beams. The enhancement levels of HC relative to EC beams are different at different momentum levels. As can be seen in both Fig. 9 and Table 3, the advantage of an HC beam is most significant at relatively low momentum levels, with its mid-span deflection over 50% smaller than its EC counterpart, i.e., HC-1 compared to EC-1. Note that, in current study, the increase in mass (clamping ends excluded) due to honeycomb filling is only about 12%, thus enabling significant improvement in specific performance. Nonetheless, as the projectile momentum is increased, the superiority of HC beam in shock resistance gradually diminishes. Meanwhile, since the inertia effect becomes more pronounced, the permanent deflections of rear and impact faces take on more curved profiles at high-momentum impacts, while their profiles are closer to a straight line at low momentum levels. The maximum core compression in the mid-span area (the region of projectile impact) of HC-1, HC-2, and HC-3 is reduced by 64.6%, 71.8%, and 87.5% relative to EC-1, EC-2, and EC-3, respectively. These results demonstrate that honeycomb filling indeed enhances the compressive strength of corrugated core, and hence is effective in resisting structural deformation with minimal increase in structural mass.

3. Numerical predictions

3.1. Numerical simulation model

Three-dimensional direct FE simulations are performed with the commercially available software ABAQUS v6.16/Explicit. Details are provided below.

3.1.1. Model description

Figure 10 displays the FE models for both EC and HC beams; due to symmetry, only quarter models are constructed. The foam projectiles are modeled with solid elements C3D8R, while the face sheets, corrugated cores, and filled honeycombs are all meshed using shell elements S4R. With the reported mesh convergence in previous research [7,8], the mesh size of foam projectiles is set as 2 mm, while the empty corrugated sandwich beams and filled honeycombs are mesh in 0.5 mm and 0.4 mm respectively. General contact is employed on all elements to simulate contact between foam projectile and impact face as well as their self-contact and is assumed frictionless. The face sheets and corrugated core, the face sheets and honeycomb blocks, and the corrugated core and honeycomb blocks are tied together to simulate braze welding and gluing. In other words, all the connections are assumed to be perfect during subsequent FE simulations. However, in Appendix A, the influence of selected interface debonding between the face sheets and core on dynamic deformations of both empty corrugated and hybrid-cored sandwich beams is quantified based on FE simulations. At the start of each simulation, a uniform initial velocity v_0 is assigned to foam projectile to hit a sandwich beam. As mentioned above, symmetry boundary

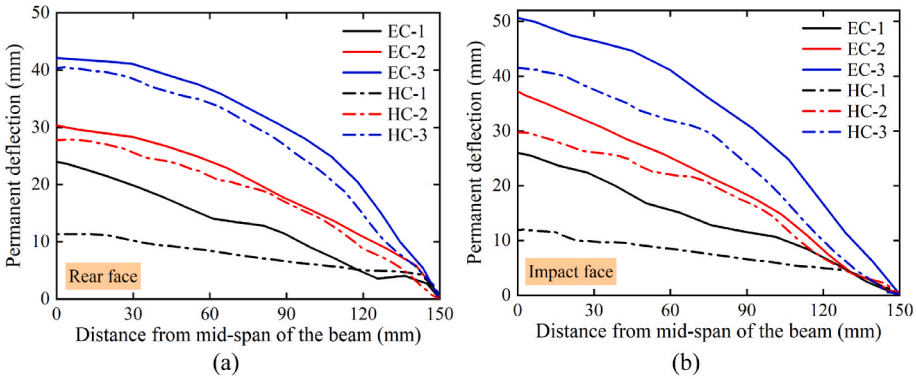

Fig. 9. Experimentally measured deflection profiles of empty corrugated sandwich beams and honeycomb-corrugation hybrid sandwich beams: (a) rear face and (b) impact face.

Table 3
Reduction ratios of mid-span deflections and maximum core compressive strain at the central area of honeycomb-corrugation hybrid sandwich beams compared to that of empty corrugated sandwich beams.

Impact impulse number	Deflection reduction ratio of rear face (%)	Deflection reduction ratio of impact face (%)	Core compression reduction ratio (%)
I-1 (for EC-1 and HC-1)	52.8	53.8	63.6
I-2 (for EC-2 and HC-2)	8.1	19.7	71.8
I-3 (for EC-3 and HC-3)	3.7	17.7	87.5

conditions are set on the FE model along the *x*-axis and *y*-axis, respectively, as shown in Fig. 10. In addition, at the end of each sandwich beam, all degrees of freedom are constrained.

3.1.2. Constitutive models

The parent material of EC beams, AISI 304 stainless steel, is modeled as an elastoplastic material. With its quasi-static mechanical behavior characterized in Section 2.1, the dynamic yield strength enhancement ratio R is employed to describe its strain-rate sensitivity. Note that the value of R is reasonably independent of the choice of equivalent plastic strain ε^{p} [50]. Therefore, with strain rate effect accounted for, the history of equivalent yield stress σ_{eq} versus equivalent plastic strain ε^{p} can be described as:

$$\sigma_{\mathrm{eq}} = R(\dot{\varepsilon}^{\mathrm{p}})\sigma_0(\varepsilon^{\mathrm{p}}), \tag{7}$$

where $\dot{\varepsilon}^{\mathrm{p}}$ is the equivalent plastic strain rate, and $\sigma_0(\varepsilon^{\mathrm{p}})$ is the quasi-static stress versus strain history. $R(\dot{\varepsilon}^{\mathrm{p}})$, which is calculated from Ref. [7], is presented in Fig. 11.

As to the parent material of aluminum honeycombs, AA3003-H18, its plastic strain rate behavior is defined using the Johnson-Cook (J-C) plasticity model, which is commonly used to describe nonlinear plastic behaviors of metallic materials with strain rate, strain hardening, and thermal softening effects considered. In the J-C model, the equivalent yield stress is expressed as:

$$\sigma_{\mathrm{eq}} = [A + B(\varepsilon^{\mathrm{p}})^n]\left[1 + C\ln\left(\frac{\dot{\varepsilon}^{\mathrm{p}}}{\dot{\varepsilon}_0}\right)\right]\left[1 - \left(\frac{T - T_{\mathrm{r}}}{T_{\mathrm{m}} - T_{\mathrm{r}}}\right)^m\right], \tag{8}$$

where the constants A, B, n, C, $\dot{\varepsilon}_0$, and m are material parameters, T is material temperature, T_{m} is melting temperature, and T_{r} is room temperature. The J-C parameters for AA3003-H18 are listed in Table 4, taken from Ref. [51].

Aluminum foam projectiles are modeled as crushable foam based on the Deshpande-Fleck (D-F) model [52] in ABAQUS, which employs an isotropic yield surface as:

$$\sigma_{\mathrm{eq}} - Y = 0, \tag{9}$$

where the equivalent yield stress σ_{eq} is given by:

$$\sigma_{\mathrm{eq}}^2 = \frac{1}{1 + (\alpha/3)^2}\left(\sigma_{\mathrm{von}}^2 + \alpha^2\sigma_{\mathrm{m}}^2\right). \tag{10}$$

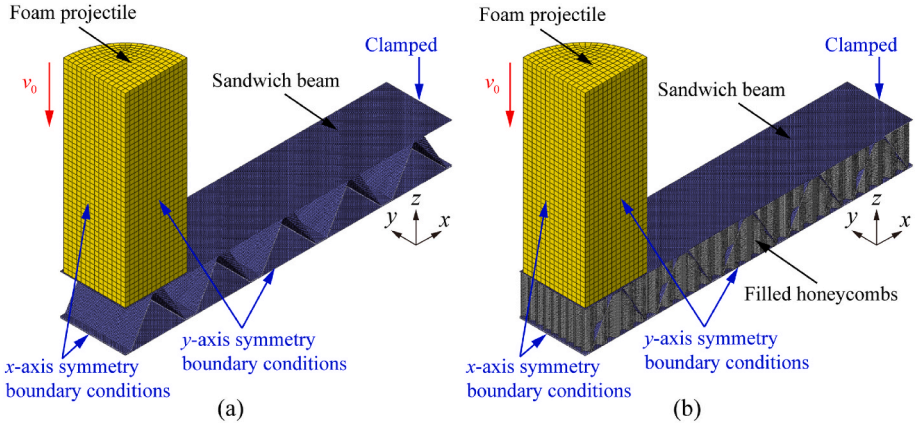

Fig. 10. Quarter finite element model of (a) empty corrugated sandwich beam and (b) honeycomb-corrugation hybrid sandwich beam.

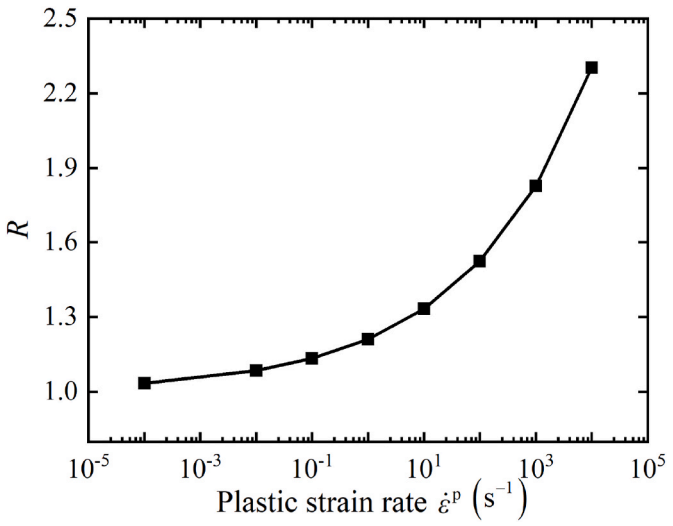

Fig. 11. Dynamic yield strength enhancement ratio R plotted as a function of equivalent plastic strain rate $\dot{\varepsilon}^{p}$ for AISI 304 stainless steel [7].

Here, α is the shape factor of the elliptical yield surface, σ_{von} is the von Mises effective stress, and σ_m is the mean stress. Additionally, according to the D-F model, the plastic Poisson ratio ν_p of metal foam can be written explicitly in terms of yield surface ellipticity α as:

$$\nu_p = \frac{(1/2) - (\alpha/3)^2}{1 + (\alpha/3)^2}. \tag{11}$$

For the aluminum foam projectiles employed in the present study, the average mass density is obtained as $\rho_p = 364.09\ \mathrm{kg/m^3}$ (detailed values for each sample are listed in Table 2), the Young's modulus is calculated as $E = 0.22\mathrm{GPa}$, the elastic Poisson ratio ν_e is fixed at 0.3 [16], while the plastic Poisson ratio ν_p is assumed as 0 [53]. The compressive behavior of foam projectiles is described using the true strain versus true stress curve converted from Fig. 3b. Besides, the strain rate effect of aluminum foam is assumed to be negligible [54].

3.2. Validation

Figure 12 displays the numerically predicted mid-span deflection versus time histories of EC-1 and HC-1, with corresponding core crushing histories presented as well. For both beam types, the deflection curves increase immediately to a maximum value and then fluctuate steadily up and down around a plateau value due to elastic springback. The mid-span deflections of rear and impact faces of EC-1 are both larger than those of HC-1. Additionally, compared to the empty beam, the core crush of the hybrid beam is reduced significantly. The permanent deflections are estimated by averaging the displacement over several cycles of elastic oscillation.

For both EC and HC beams, the estimated permanent deflections are compared with experimental results in Fig. 13. To a reasonable approximation, the predictions are consistent with experimental measurements and, as the momentum is increased, the predicted permanent mid-span deflections exhibit a similar variation trend with experimental observations. The difference (less than 20% in all cases) between numerical and experimental results may be attributed to: (i) manufacturing defects and added mass of both braze alloy and glue are not considered; (ii) clamped and symmetric boundary conditions assumed in FE models may not fully represent real experimental situations; (iii) debonding of brazing joints and gluing interfaces is not considered in FE simulations.

Figure 14 compares the experimental observed and FE predicted final deformation profiles of EC and HC beams. The large inelastic deformation, core compression, and core shear of EC beams as well as the large inelastic deformation and slight core compression at high momentum level of HC beams are predicted accurately by FE simulations. Though interfacial failure is ignored in the present study, the numerically predicted results agree well with experimental measurements.

Contact pressure between foam projectile and impact face is extracted and presented in Fig. 15 for both EC and HC beams. The pressure increases suddenly from zero to a peak after the impact of foam projectile and subsequently decreases to zero in 1.5 ms, as shown in Figs. 15a and d. The curves of EC and HC beams exhibit similar overall variation trends. Upon integrating the pressure versus time history, the impact impulse per unit area transferred by foam projectile to impact face is obtained, as shown in Figs. 15b and e, which increases rapidly after the impact and then gradually reaches the final stable value. Dividing the final transferred impact impulse by initial projectile momentum allows calculating the transferred ratio, and the results are presented in Figs. 15c and f. In all cases studied here, the transferred ratio is close to 1, indicating that the transferred impact impulse is approximately the same as the initial projectile momentum. In other words, it is reasonable to judge the impact impulse directly from initial projectile momentum for both EC and HC beams.

3.3. Discussion

Thus far, significantly enhanced impact resistance of end-clamped hybrid sandwich beams has been captured both experimentally and numerically. In addition, the 3D FE models constructed could accurately predict the dynamic responses of both empty and hybrid sandwich beams. In this section, further FE simulations are performed to explore how impact velocity, honeycomb relative density, and honeycomb core

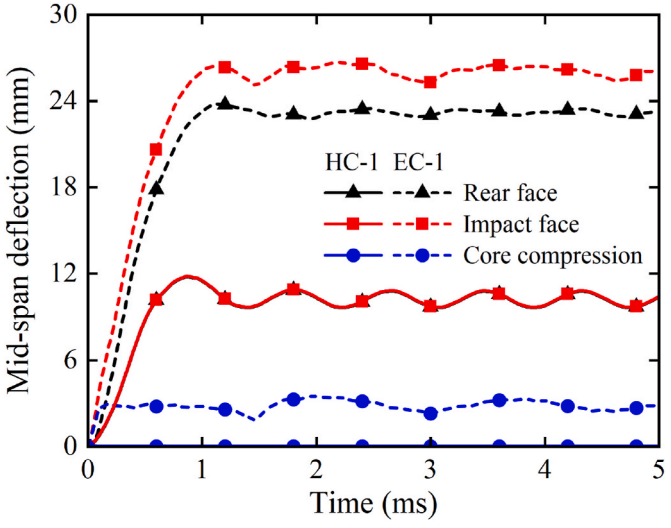

Fig. 12. Numerically predicted mid-span deflection versus time histories and corresponding core crush histories of EC-1 and HC-1.

Table 4
Johnson-Cook plasticity model parameters of AA3003-H18 [51].

Material	Density (kg/m^3)	Young's modulus (GPa)	Poisson's ratio	A (MPa)	B (MPa)	n	C	$\dot{\varepsilon}_0$ (s^{-1})	m
AA3003-H18	2680	67.6	0.33	214	143	0.36	0.015	1	0

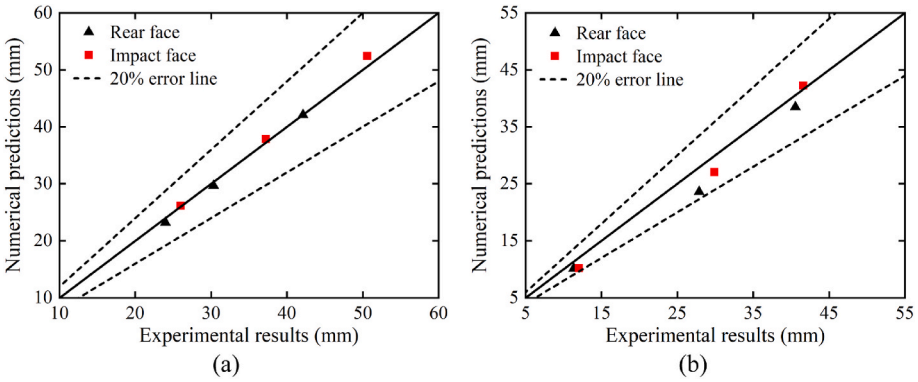

Fig. 13. Numerically predicted permanent mid-span deflections compared with experimental results: (a) empty corrugated sandwich beams and (b) honeycomb-corrugation hybrid sandwich beams.

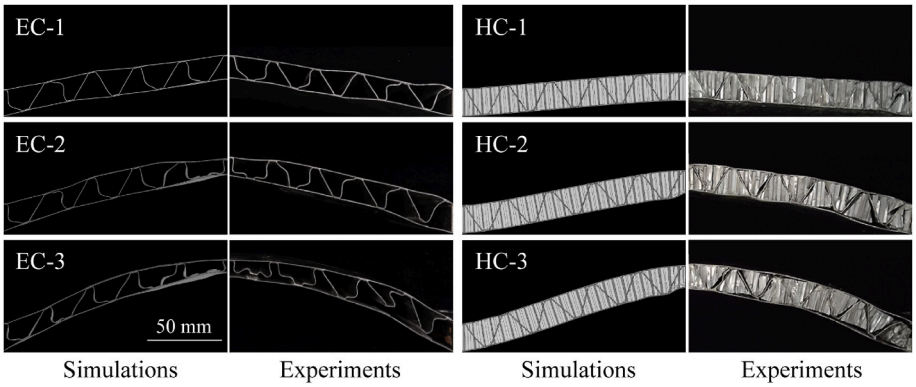

Fig. 14. Experimentally measured and numerically predicted final deformation profiles of empty corrugated and hybrid sandwich beams.

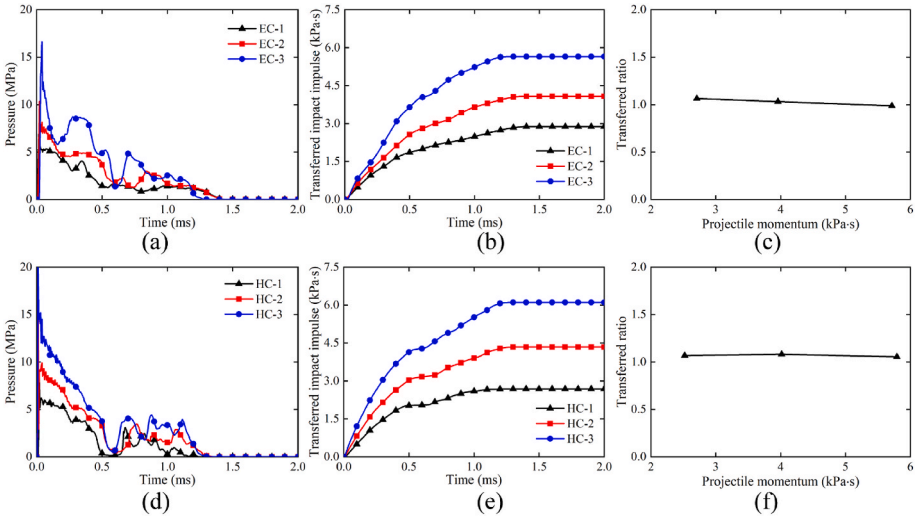

Fig. 15. Empty corrugated sandwich beams: (a) numerically predicted pressure versus time histories, (b) transferred impulse versus time histories, and (c) corresponding transferred ratio. Hybrid-cored sandwich beams: (d) numerically predicted pressure versus time histories, (e) transferred impulse versus time histories, and (f) corresponding transferred ratio.

orientation affect the impact resistance of hybrid sandwich beams. The density of foam projectiles is fixed at 364.09 kg/m^3, the average value of experimental tests.

3.3.1. *Impact velocity of foam projectile*

For both empty and hybrid sandwich beams, Fig. 16 displays the effect of impact velocity on mid-span deflections of both rear and impact faces, the reduction of mid-span deflection, and the core compressive strain. The foam projectile is accelerated to 50, 100, 150, 200, and 250 m/s sequentially to control its initial momentum. As shown in Figs. 16a and b, the HC beams exhibit a significant advantage in mid-span deflections for all impact velocities studied here. However, the advantage gradually diminishes with increasing impact velocity, especially for the rear face. Figure 16c compares the reduction in mid-span deflection of

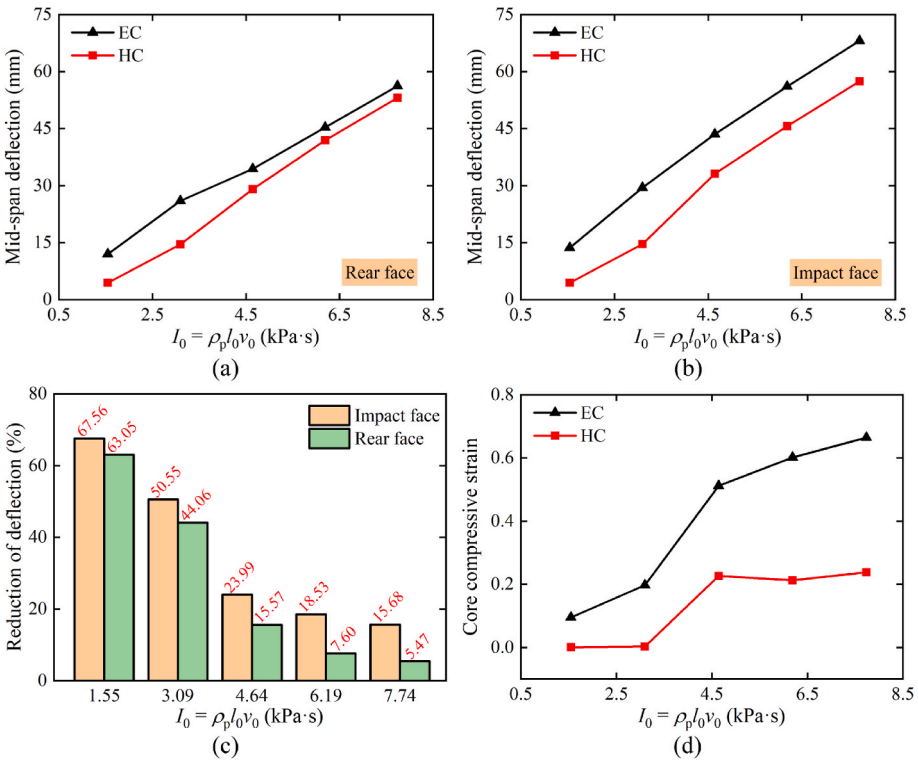

Fig. 16. Effect of impact velocity on mid-span deflection of (a) rear face and (b) impact face, (c) reduction in mid-span deflection, and (d) core compressive strain located in impact region: comparison between empty corrugated and hybrid-cored sandwich beams.

HC beams with that of EC beams at different impact velocities. With the increase of impact velocity, the advantage of HC beams decreases from 67.56% to 15.68% for the impact faces, and from 63.05% to 5.47% for the rear faces. Interestingly, as displayed in Fig. 16d, the core compressive strains at the impact region of HC beams are far less than those of HC beams, though both increase with increasing impact velocity.

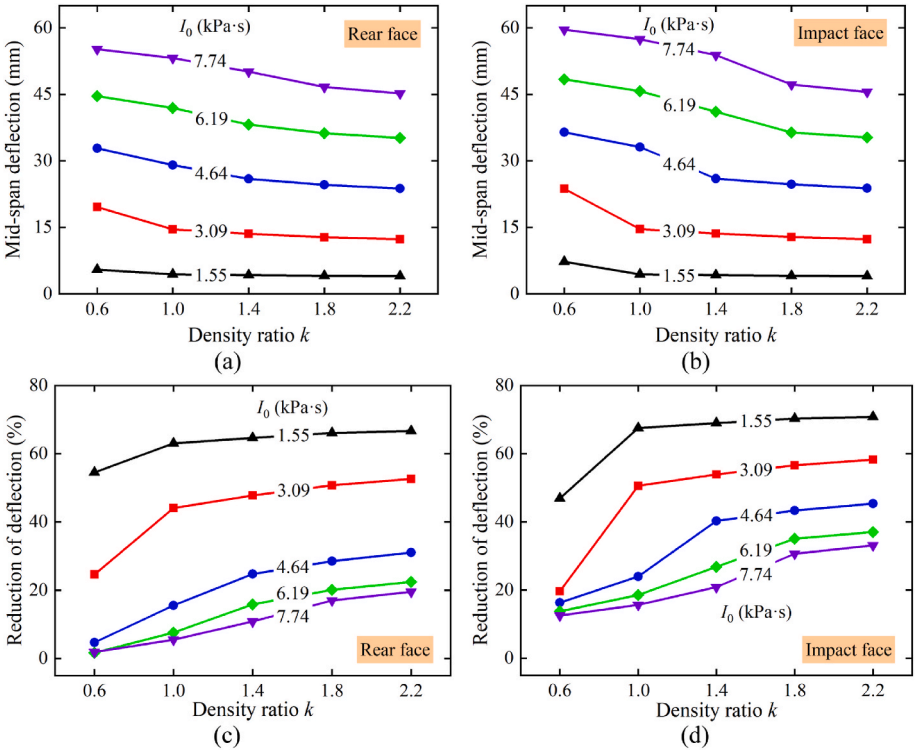

Fig. 17. Effect of honeycomb relative density on mid-span deflection of (a) rear and (b) impact faces at selected impact velocities as well as on reduction of mid-span deflection of (c) rear and (d) impact faces relative to empty corrugated sandwich beams subjected to identical velocity impacts.

3.3.2. Relative density of honeycomb filling

As captured through the present experimental tests and numerical simulations, the core crush and shear deformation of HC beams are mitigated significantly due to considerable enhancement in out-of-plane compressive strength and longitude shear strength of the hybrid core via honeycomb filling. The relative density of honeycomb insertions plays an important role in the mechanical performance of honeycomb-corrugation hybrid core. Thus, in this section, how the relative density of honeycombs affects the impact resistance of HC beams is quantified. For simplification, the relative density of honeycombs is controlled by varying cell wall thickness. With the cell wall thickness t_{h0} (= 0.05 mm) adopted in experiments set as the reference, the density ratio k is defined as:

$$k = \frac{\overline{\rho}_h}{\overline{\rho}_{h0}} = \frac{t_h}{t_{h0}}, \tag{12}$$

where $\overline{\rho}_{h0}$ is the reference relative density of honeycombs.

Figures 17a and b displays the effect of honeycomb relative density on mid-span deflections of HC beams at various impact velocities (consistent with Section 3.3.1). The results suggest that while the mid-span deflections of both rear and impact faces decrease with increasing relative density, the deflection of impact face is more sensitive, which may be attributed to core crush. Figures 17c and d presents the reduction ratio of mid-span deflection of HC beams relative to EC beams subjected to the same impact velocities. For both rear and impact faces, the reduction ratio increases with increasing relative density. When the density ratio k is greater than 1, the increase of reduction ratio is gradually moderated as projectile momentum is decreased. In addition, regardless of honeycomb relative density, the advantage in shock resistance of hybrid sandwich beams decreases significantly as projectile momentum is increased.

3.3.3. Orientation of honeycomb filling

Honeycombs are known to be anisotropic, thus it is of importance to study the influence of honeycomb orientation on impact resistance. Generally, a local coordinate system T-L-W is defined for hexagonal honeycombs. As shown in Fig. 18a, W is along the expansion direction, L is along the ribbon direction, and T is along the cell depth direction. For variable control, it is noticed that different honeycomb filling orientations have approximately the same out-of-plane compressive strength while a slight difference in in-plane shear strength [55]. Figure 18a illustrates further the two filling orientations: LT refers to the case when the L-direction of filled honeycombs is along the x-direction of global coordinate while the T-direction is along the z-direction; WT refers to the case when the W-direction of filled honeycombs is along the x-direction of global coordinate while the T-direction is along the z-direction. The sensitivity of in-plane shear strength of honeycomb-corrugation hybrid core to the orientation of honeycomb filling is presented in Appendix B.

Numerical simulations of HC beams with two honeycomb filling orientations (i.e., LT and WT) are firstly performed at $I_0 = 2.52$ kPa·s, for at this momentum the HC beam exhibits the best enhancement compared with EC beams in experimental tests. The numerically predicted permanent deflections of rear and impact faces are presented in Fig. 18b for HC beams with both LT and WT filling orientations. In all cases, there is almost no core crush as the beams have approximately the same out-of-plane compressive strength. However, slight difference in permanent deflections is observed. The permanent deflections with LT filling are ~11% smaller than that with WT filling.

In Fig. 18c, the reduction of mid-span deflection with WT filling is compared with that with LT filling for selected impact velocities. Due to similar core compressive strains of HC beams with two different filling orientations, only rear face mid-span deflection is displayed. It is seen that the reduction of mid-span deflection increases firstly at relatively low momentum levels and then decreases as projectile momentum is increased.

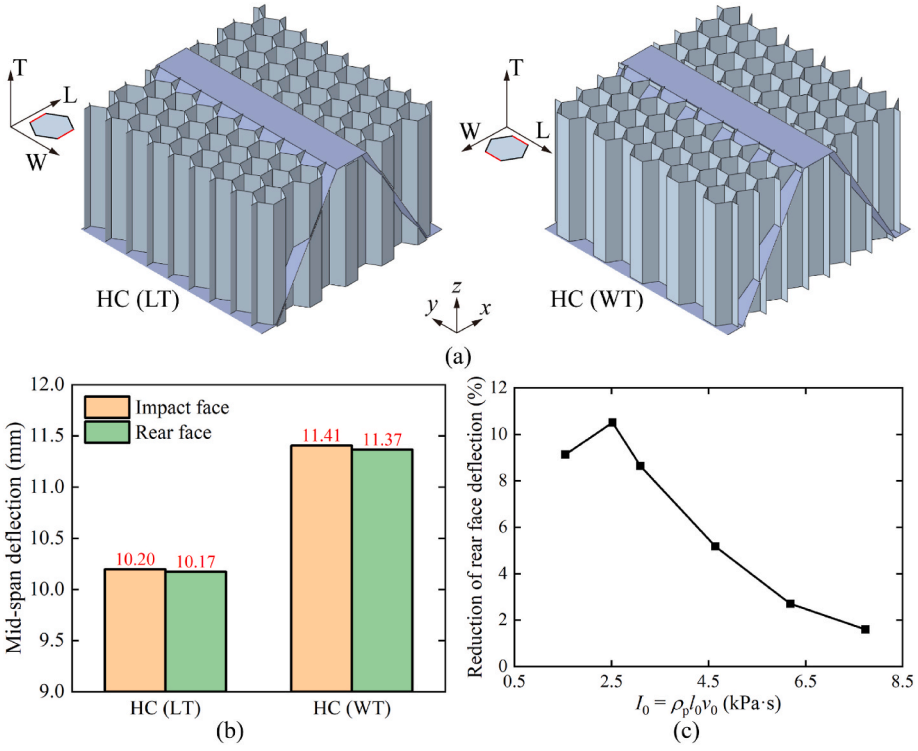

Fig. 18. (a) Sketch of hybrid cores with LT and WT filling orientations; (b) numerically predicted permanent mid-span deflections of hybrid sandwich beams with LT and WT filling orientations for $I_0 = 2.52$ kPa·s; (c) reduction of rear face deflection of hybrid sandwich beam with LT filling orientation compared to that with WT filling orientation for selected impact momentum levels.

4. Enhancement mechanisms

Thus far, the dynamic responses of corrugation-honeycomb hybrid sandwich beams are systematically investigated both experimentally and numerically, and the influence of several key factors is revealed. Four major phenomena are captured: (i) hybrid sandwich beams exhibit significant shock resistance advantage over empty corrugated sandwich beams, with minimal increase in total mass; (ii) the advantage of hybrid sandwich beams diminishes with increasing projectile momentum; (iii) filling stronger honeycombs (with higher relative density) contributes to smaller core crush and more reduction of mid-span deflections; (iv) honeycomb filling along the orientation corresponding to stronger longitudinal shear strength has greater advantage in shock resistance, particularly at relatively low projectile momentums.

Based on the classical three-stage decoupled theory of sandwich beams subjected to shock loadings [1,56] and observations in the current study, Fig. 19 illustrates schematically the various deformation stages of a sandwich beam subjected to shock loading over a central patch. The impulse over the central patch is imparted to the front face at stage I (Fig. 19a), causing it to acquire a velocity and compress the core at stage II (Fig. 19b). Due to deformation mismatch between impact and rear faces at the edges of local impact region, longitudinal shear of the core occurs. Subsequently, movement of the impact face slows down due to core crushing resistance while the rear face is accelerated due to dynamic core compression. At the end of core crush, the rear and impact faces acquire a consistent velocity to deform overall, comprising a combination of beam bending and longitudinal stretching (stage III, Figs. 19c–e). In the beginning, based on the yield criterion in reference to the combination of plastic bending moment (M) and plastic membrane force (N) of the beam, plastic hinges are initiated and then propagate towards the mid-span and supports (Fig. 19c). Meanwhile, during the propagation of plastic hinges, longitudinal shear of the core is generated across the span of beam along with the propagation paths of these hinges (Fig. 19d). Upon arriving at the mid-span and supports of beam, the plastic hinges become stationary, with the beam continuously bending and stretching until its velocity reduces to zero (Fig. 19e).

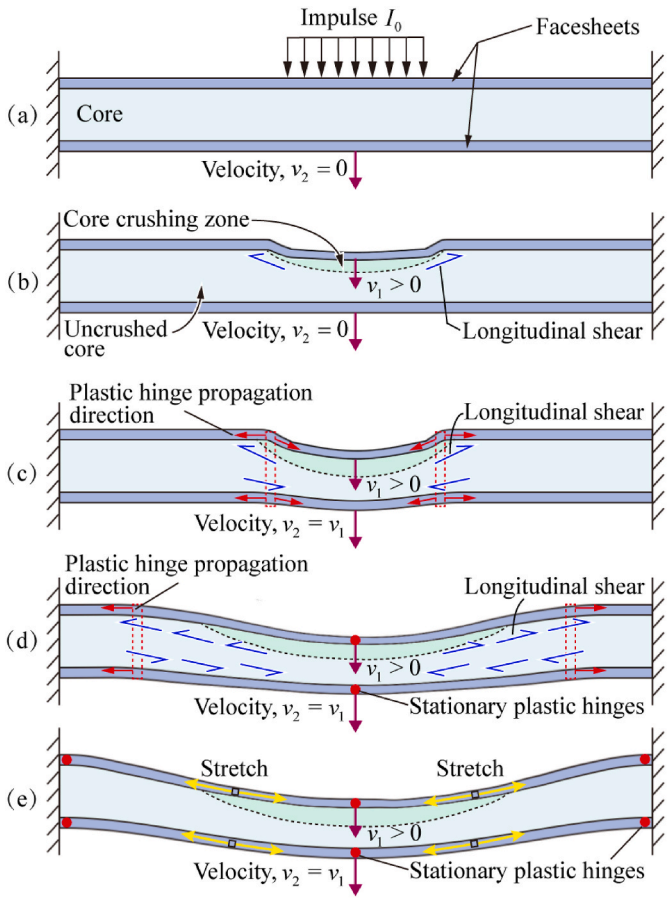

Fig. 19. Schematic illustration of a sandwich beam subjected to shock loading over a central patch: (a) impulse loading (stage I); (b) core crushing (stage II); (c) overall deformation (stage III) dominated by bending, wherein the rear face is accelerated and plastic hinges are initiated and beginning to propagate towards mid-span and supports of beam, (d) overall deformation (stage III) dominated by bending, combined with longitudinal core shear across beam span along with the propagation paths of plastic hinges; (e) overall deformation (stage III) dominated by stretch.

For the plastic hinges, the shape of the yield surface for a sandwich beam in (N, M) space depends upon the morphology of the core and the relative strength and thickness of the face sheets and core. Correspondingly, the combined bending and stretching yield locus is described by [1]:

$$|m| + |n| = 1, \tag{13}$$

where $m = M/M_p$ and $n = N/N_p$, M_p and N_p being the plastic bending moment and plastic membrane force of sandwich beam, respectively, given by:

$$M_p = \sigma_{fY} t_f \left(h_c + t_f\right) + \sigma_{lY} \frac{h_c^2}{4}, \tag{14}$$

$$N_p = \sigma_{lY} h_c + 2\sigma_{fY} t_f. \tag{15}$$

Here, σ_{fY} and σ_{lY} are the yield strength of face sheets and longitudinal strength of core, respectively. For a compressed cross-section with an average core compressive strain ε_c, the plastic membrane force is insensitive to core compression [1]. Therefore, the plastic membrane force for the compressed cross-section can be written as:

$$N_p^{'} = N_p = \sigma_{lY} h_c + 2\sigma_{fY} t_f, \tag{16}$$

while the plastic bending moment is expressed by:

$$M_p^{'} = \sigma_{fY} t_f \left[h_c(1-\varepsilon_c) + t_f\right] + \sigma_{lY} \frac{h_c^2(1-\varepsilon_c)}{4}. \tag{17}$$

Thus, the yield locus for a compressed sandwich cross-section in (N, M) space is given by:

$$|m^{'}| + |n^{'}| = 1, \tag{18}$$

where $m^{'} = M/M_p^{'}$ and $n^{'} = N/N_p^{'}$.

Additionally, as reported before, when the deflection of a sandwich beam is small, its dynamic response is dominated by bending moment; for larger deflections, however, the effect of membrane force becomes more critical [56]. Further, when the mid-span deflection exceeds the initial beam height of H, the membrane force even dominates the structural response [57].

For honeycomb-corrugation sandwich beams studied here, the enhanced core compressive strength reduces significantly core compressive strain ε_c over the central patch, as demonstrated by experimental and numerical results of the previous sections. Therefore, the plastic bending moment at compressed cross-section is significantly increased (see Equation (17)), contributing to the extension of the yield surface. However, with the increase of initial momentum, the amount of mid-span deflection is mainly dominated by membrane forces. As shown in Equation (15) and (16), the contribution of core to plastic membrane force is negligible compared to face sheets, since $\sigma_{lY} h_c$ is not on the same order of magnitude as $2\sigma_{fY} t_f$. Therefore, the advantage of hybrid sandwich beams in shock resistance diminishes at relatively large momentum levels. Meanwhile, as the longitudinal shear of core across beam span dissipates a portion of the energy as illustrated in Fig. 19, improving the shear strength of hybrid core also contributes to

enhancing the shock resistance. However, as the momentum is increased, the effect of core longitudinal shear weakens significantly due to the decay of core contribution.

Note that, the enhancement mechanisms proposed here are not specific for honeycomb-corrugation sandwich beams, valid also for alternative hybrid-cored sandwich constructions under shock loadings. In previous studies, hybrid-cored sandwich constructions with a variety of filling materials (e.g., water [7], sand particles [8], and foams [5,6]) were reported to exhibit enhanced shock resistance as well. It was argued that the reduced compressive strain ε_c, as a result of the elevated compressive strength due to hybrid design, led to enhanced plastic bending strength and hence enlarged yield surface of the sandwich construction: this may be one of the main mechanisms underlying the enhanced shock resistance. However, for a sandwich beam filled with either water or sand, such enhancement is again unappealing as the corresponding increase in mass is also significant. As for the foam-filled sandwiches, addressing the issue of matching in mechanical performance between sub-structures (e.g., foam filling and corrugated members) is of importance. For example, compared with aluminum honeycombs, the filled aluminum foam requires a higher relative density for the hybrid-cored sandwich to achieve the same level of performance enhancement. Detailed comparisons and discussions are presented in Section 5.

5. Comparison with competing sandwich constructions

One of popular hybrid lightweight cellular constructions is foam-filled hybrid structures, which have been proved to be advantageous in energy absorption [9,58] and dynamic resistance [5,6]. In this section, based upon FE simulation results, the dynamic responses of honeycomb-corrugation sandwich beams are compared with aluminum foam-filled corrugated sandwich beams. For consistency, the relative density $\overline{\rho}_p$ of filled aluminum foams is the same as that of honeycombs. Additionally, the shock resistance performance of the original sandwich construction, i.e., empty corrugated sandwich beam with consistent mass (thickness t_c of corrugated members set as 0.64 mm) is also compared.

For close-celled aluminum foams, the Young's modulus E_p, yield strength σ_p, nominal densification strain ε_D, and strain hardening (expressed as engineering stress versus strain curve) are calculated as functions of foam relative density according to a series of empirical formulas experimentally validated by Hanssen et al. [59], as:

$$\left\{E_p, \sigma_p, \eta, 1/\lambda, \kappa\right\} = C_0 + C_1 \overline{\rho}_p^n, \tag{19}$$

$$\sigma_n = \sigma_p + \kappa \frac{\varepsilon_n}{\varepsilon_D} + \eta \ln\left[\frac{1}{1-(\varepsilon_n/\varepsilon_D)^{\lambda}}\right], \tag{20}$$

where C_0, C_1, n, η, λ, and κ are material coefficients, with specific values summarized in Table 5 [59]. Besides, for aluminum foams with different relative densities, the Poisson ratio is fixed at 0.3 [16], and the nominal densification strain is taken as $\varepsilon_D = 1 - 1.4\overline{\rho}_p$ [60].

Figure 20 compares the mid-span deflections of rear and impact faces among empty corrugated sandwich beams, honeycomb-corrugation sandwich beams, and aluminum foam-filled corrugated sandwich beams of equal mass. With the range of initial projectile momentum and the density of sandwich cores studied here, the mid-span deflection of the HC beam is consistently smaller than those of the other two constructions, thus demonstrating its superiority for shock resistance enhancement. For the aluminum foam-filled sandwich beam, the advantage in shock resistance is small in comparison with the EC beam, because the filled foam has a low relative density such that its mechanical properties are too weak to reduce the core compressive strain or, equivalently, enlarge the yield surface of the foam-filled sandwich. To further elevate the shock resistance of the aluminum foam-filled sandwich, the relative density of the foam needs to be increased, but the corresponding increase in total mass becomes another issue to be addressed. Meanwhile, the superiority of HC beam diminishes as projectile momentum becomes sufficiently large, because the contribution of its core in the stretching stage is much less than its face sheets, which is consistent with the enhancement mechanisms discussed in Section 4.

Table 5
Material coefficients of aluminum foam based on the hardening model [59].

Model description for aluminum foam: $\{E_p, \sigma_p, \eta, 1/\lambda, \kappa\} = C_0 + C_1\overline{\rho}_p^n$					
Coefficients	E_p (GPa)	σ_p (MPa)	η (MPa)	$1/\lambda$	κ (MPa)
C_0	0	0	0	0.1	0
C_1	330	720	251	15.7	42
n	2.45	2.33	1	3	1.42

6. Concluding remarks

The main motivation of this study is to achieve the excessive improvement of dynamic resistance performance over a percentage increase in mass of corrugated sandwich beams through the honeycomb-filling. Dynamic responses of honeycomb-corrugation hybrid sandwich beams under simulated shock loadings with aluminum foam projectiles are investigated experimentally. FE numerical models are established and validated with experimental measurements. Some key factors are discussed based on the validated numerical models to reveal their effects on beam shock resistance, with the enhancement mechanisms analyzed and summarized. Finally, the shock resistance of honeycomb-corrugation hybrid sandwich beams is compared with aluminum foam-filled and empty corrugated sandwich beams under equal mass conditions. Main conclusions are summarized below.

(i) Honeycomb filling significantly enhances the shock resistance of corrugated sandwich beams, especially at relatively low projectile momentum levels, where the advantage is much more than the mass increase compared to empty corrugated sandwich beams. However, the shock resistance advantage of hybrid sandwich beams diminishes with projectile momentum increases.
(ii) Honeycombs with higher relative density are responsible for smaller mid-span deflection of beams, while the enhancement is both inconspicuous at relatively high projectile momentum. Meanwhile, filling honeycombs with higher longitudinal shear strength orientation (the compressive strength keeps consistent) is more efficient for shock resistance.
(iii) Three main mechanisms are considered responsible for the enhancement of honeycomb-corrugation hybrid sandwich beams based on the classical three-stage decoupling theory: (a) The expanded yield surface owned to the enhanced plastic bending moment at compressed cross-section of beams contributes to the enhancement of shock resistance of hybrid beams; (b) The higher longitudinal shear strength of honeycomb-corrugation hybrid cores makes a contribution on the shock resistance as well; (c) The transfer from bending-dominated to stretching-dominated stage with projectile momentum increases leads to the diminishment of the shock resistance advantage.
(iv) When subjected to shock loading, the present honeycomb-corrugation hybrid sandwich constructions exhibit significant advantage in shock resistance relative to foam-corrugation sandwiches having equal mass, because the filled aluminum honeycombs match better in mechanical performance with the metallic corrugation members than the filled aluminum foams at the studied relative density of this work.

CRediT authorship contribution statement

Zengshen Yue: Conceptualization, Investigation, Methodology,

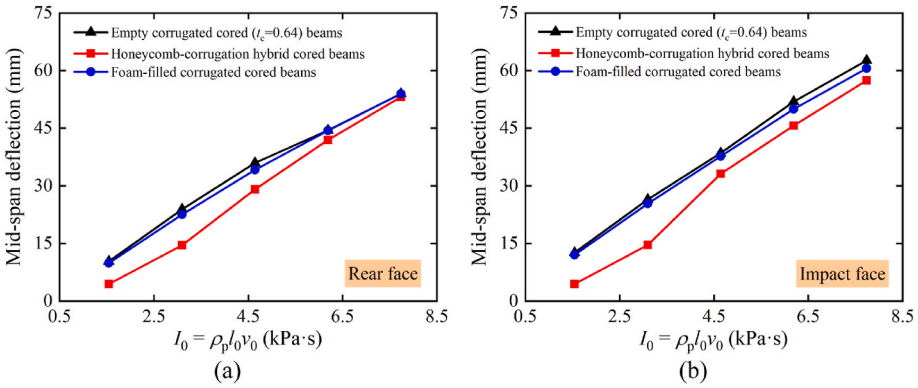

Fig. 20. Numerically predicted mid-span deflections of empty corrugated sandwich beam, honeycomb-corrugation hybrid sandwich beam, and aluminum foam-filled corrugated sandwich beam for selected initial projectile momentums: (a) rear face; (b) impact face. The sandwich beams are considered to have equal mass.

Software, Visualization, Writing – original draft. **Xin Wang:** Conceptualization, Methodology, Writing – review & editing. **Chao He:** Investigation, Data curation. **Runpei Yu:** Methodology. **Xue Li:** Methodology. **Zhenyu Zhao:** Funding acquisition, Software. **Qiancheng Zhang:** Supervision, Writing – review & editing. **Tian Jian Lu:** Supervision, Funding acquisition, Writing – review & editing.

Declaration of competing interest

The authors declare that they have no known competing financial interests or personal relationships that could have appeared to influence the work reported in this paper.

Data availability

The authors do not have permission to share data.

Acknowledgments

This work is supported by the National Natural Science Foundation of China (11972185, 12072250, and 12002156) and the Open Fund of the State Key Laboratory of Mechanics and Control of Mechanical Structures (MCMS-I-0222K01). XW thanks China Scholarship Council for a two-year scholarship (202006280483) as a visiting student at National University of Singapore.

Appendix A. Influence of interface debonding on structural deformation

The effects of interface debonding between the face sheets and core on the dynamic structural deformations of both empty corrugated sandwich beams (EC) and honeycomb-corrugation hybrid cored sandwich beams (HC) are numerically analyzed here. With reference to Fig. A1, selected welding (or gluing) areas where interface failure occurred in impact experiments are purposely left unbonded in FE simulations, as marked by red lines in the figure. Quantitatively, the area of debonding interfaces accounts for 30% and 13% of the total connected interface area of the EC and HC beams, respectively. Based upon the verified FE model in Section 3.1, foam projectiles with a density of 364.09 kg/m^3 are assigned to dynamically hit both the EC and HC sandwich beams, at five different impact velocities (50, 100, 150, 200, 250 m/s). For both the EC and HC beams, Fig. A2 presents the mid-span permanent deflections of the rear and impact faces. The results show that, although debonding of the considered interfaces increases the structural deformation, the increase is marginal. Therefore, for the problem considered, neglecting the interface debonding is considered reasonable, as the focus of the current study has been placed upon revealing the enhancement advantage and interrogating the mechanisms by which honeycomb filling realizes its mitigation effect on structural deformation.

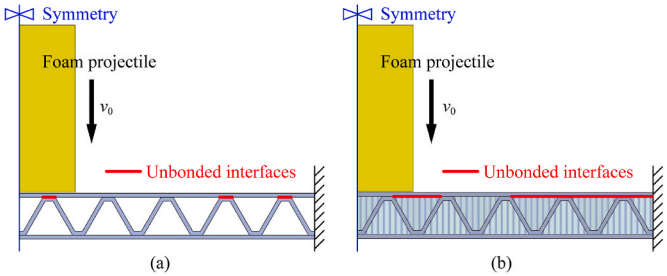

Fig. A1. FE model of sandwich beam with selected unbonded interfaces: (a) empty corrugated sandwich beam (EC), and (b) honeycomb-corrugation hybrid-cored sandwich beam (HC).

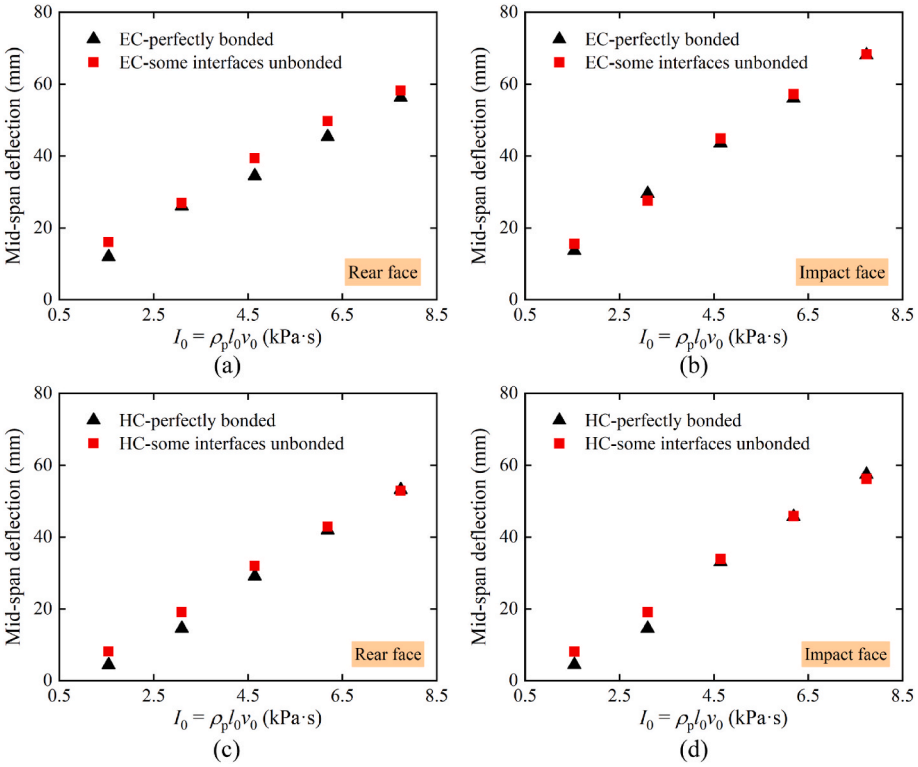

Fig. A2. Effect of debonding at selected interfaces where interface failure occurred during impact experiments on: (a) rear face deflection and (b) impact face deflection of EC; (c) rear face deflection and (d) impact face deflection of HC.

Appendix B. Quasi-static in-plane shear behaviors of sandwich structures: comparison among three different core configurations

Similar to Section 3.3.3, a local coordinate system T-L-W is defined for hexagonal honeycombs as shown in Fig. B1a, where W is along the expansion direction, L is along the ribbon direction, and T is along the cell depth direction. Quasi-static in-plane shear responses of both the empty corrugated core and honeycomb-corrugation hybrid core are calculated via FE simulations with ABAQUS v6.16/Explicit. Honeycomb-corrugation hybrid core with either LT or WT honeycomb orientation is considered (LT: the L-direction of filled honeycombs is along the *x*-direction of global coordinate while the T-direction is along the *z*-direction; WT: the W-direction of filled honeycombs is along the *x*-direction of global coordinate while the T-direction is along the *z*-direction). Due to periodicity along the *x* and *y*-directions of these sandwich constructions, representative volume element (RVE) models are employed to simulate their mechanical characteristics. As shown in Fig. B1a, the RVE regions are surrounded by red dashed lines. For each model, periodic boundary conditions are set along the *x* and *y*-directions; the bottom face sheet is fixed, the top face sheet can move along the *x*-direction, and any other freedom is constrained. The loading velocity is set as 1 mm/ms. Additionally, the face sheets and corrugated core, the face sheets and honeycomb blocks, and the corrugated core and honeycomb blocks are assumed to be ideally connected.

The numerically calculated in-plane shear stress versus shear strain histories are presented in Fig. B1b. Corresponding shear deformations located at the hollow dots marked in Fig. B1b are illustrated in Fig. B1c. The shear response of empty corrugated core exhibits an initial elastic response until the peak strength. Subsequently, a sudden drop occurs, followed by a slow hardening response. The hybrid cores with both LT and WT honeycomb orientations exhibit an initial elastic response, followed by a nonlinear slow hardening stage.

Consider next the typical shear deformations of the three core configurations discussed above. The empty corrugated core collapses by Euler elastic buckling of its member on the compression side. Subsequently, core crushing is governed by the rotation of three plastic hinges, which are marked by red dots in Fig. B1c. However, for hybrid cores with both LT and WT honeycomb orientations, more plastic hinges (marked by red dots in Fig. B1c) form on the initially compressed side of the corrugation member. In addition, shear buckling occurs in the honeycomb blocks within a wide (rather than quite localized and narrow) region. This may be attributed to the mutual deformation constraints of inserted honeycombs and corrugation members, which improve the buckling resistance of both constituents, thus enabling the shear strength of the hybrid core to be significantly enhanced. Additionally, some cell walls of the LT honeycomb-corrugation hybrid core are parallel to the shear loading direction, which contribute to its higher load-carrying efficiency. Therefore, the hybrid core with the LT honeycomb orientation possess stronger shear resistance than that with the WT honeycomb orientation: quantitatively, the $\tau_{LT} \sim \gamma_{LT}$ response is about 10–20% stronger compared to the $\tau_{WT} \sim \gamma_{WT}$ response under consistent shear strains.

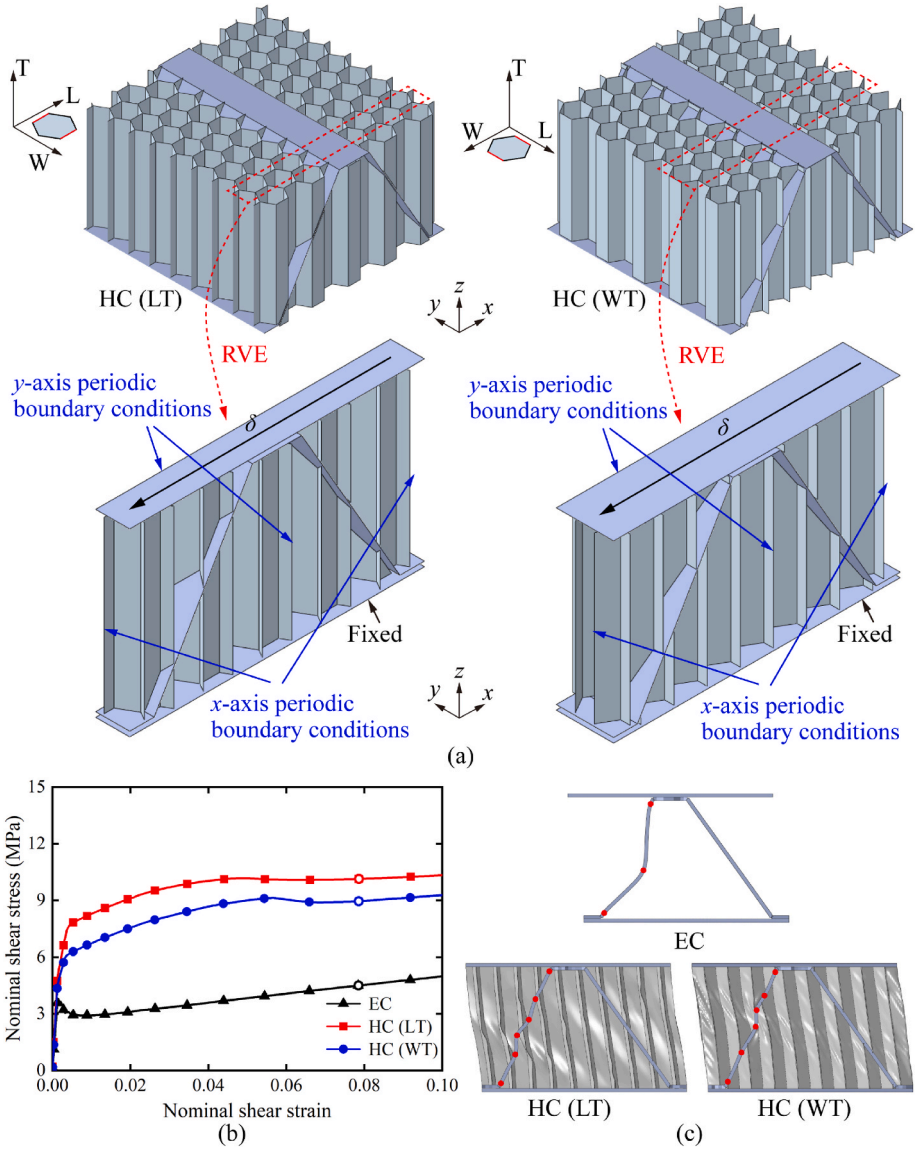

Fig. B1. (a) Repredeentative volume element (RVE) models for in-plane shear simulation of honeycomb-corrugation hybrid cores with LT and WT honeycomb orientations; (b) numerically predicted shear stress versus strain responses of empty corrugated core and honeycomb–corrugation hybrid cores with LT and WT honeycomb orientations; (c) comparison of shear deformations at locations marked by hollow dots in (b) for three different cores.

References

[1] Fleck NA, Deshpande VS. The resistance of clamped sandwich beams to shock loading. J Appl Mech Trans ASME 2004;71:386–401. https://doi.org/10.1115/1.1629109.

[2] Rathbun HJ, Radford DD, Xue Z, He MY, Yang J, Deshpande V, et al. Performance of metallic honeycomb-core sandwich beams under shock loading. Int J Solid Struct 2006;43:1746–63. https://doi.org/10.1016/j.ijsolstr.2005.06.079.

[3] Peng C, Tran P. Bioinspired functionally graded gyroid sandwich panel subjected to impulsive loadings. Compos B Eng 2020;188:107773. https://doi.org/10.1016/j.compositesb.2020.107773.

[4] Wang X, He C, Yue Z, Li X, Yu R, Ji H, et al. Shock resistance of elastomer-strengthened metallic corrugated core sandwich panels. Compos B Eng 2022;237:109840. https://doi.org/10.1016/j.compositesb.2022.109840.

[5] Zhang P, Cheng Y, Liu J, Li Y, Zhang C, Hou H, et al. Experimental study on the dynamic response of foam-filled corrugated core sandwich panels subjected to air blast loading. Compos B Eng 2016;105:67–81. https://doi.org/10.1016/j.compositesb.2016.08.038.

[6] Cheng Y, Liu M, Zhang P, Xiao W, Zhang C, Liu J, et al. The effects of foam filling on the dynamic response of metallic corrugated core sandwich panel under air blast loading – experimental investigations. Int J Mech Sci 2018;145:378–88. https://doi.org/10.1016/j.ijmecsci.2018.07.030.

[7] Wang X, Yu R-P, Zhang Q-C, Li L, Li X, Zhao Z-Y, et al. Dynamic response of clamped sandwich beams with fluid-fillied corrugated cores. Int J Impact Eng 2020;139:103533. https://doi.org/10.1016/j.ijimpeng.2020.103533.

[8] Yu RP, Wang X, Zhang QC, Li L, He SY, Han B, et al. Effects of sand filling on the dynamic response of corrugated core sandwich beams under foam projectile impact. Compos B Eng 2020;197:108135. https://doi.org/10.1016/j.compositesb.2020.108135.

[9] Yan LL, Yu B, Han B, Chen CQ, Zhang QC, Lu TJ. Compressive strength and energy absorption of sandwich panels with aluminum foam-filled corrugated cores. Compos Sci Technol 2013;86:142–8. https://doi.org/10.1016/j.compscitech.2013.07.011.

[10] Han B, Qin K, Yu B, Wang B, Zhang Q, Lu TJ. Honeycomb-corrugation hybrid as a novel sandwich core for significantly enhanced compressive performance. Mater Des 2016;93:271–82. https://doi.org/10.1016/j.matdes.2015.12.158.

[11] Tang Y, Ren S, Meng H, Xin F, Huang L, Chen T, et al. Hybrid acoustic metamaterial as super absorber for broadband low-frequency sound. Sci Rep 2017;7:43340. https://doi.org/10.1038/srep43340.

[12] Sun S, Feng S, Zhang Q, Lu TJ. Forced convection in additively manufactured sandwich-walled cylinders with thermo-mechanical multifunctionality. Int J Heat Mass Tran 2020;149:119161. https://doi.org/10.1016/j.ijheatmasstransfer.2019.119161.

[13] Ni CY, Hou R, Xia HY, Zhang QC, Wang WB, Cheng ZH, et al. Perforation resistance of corrugated metallic sandwich plates filled with reactive powder concrete:

experiment and simulation. Compos Struct 2015;127:426–35. https://doi.org/10.1016/j.compstruct.2015.02.059.
[14] Ni CY, Li YC, Xin FX, Jin F, Lu TJ. Ballistic resistance of hybrid-cored sandwich plates: numerical and experimental assessment. Compos Part A Appl Sci Manuf 2013;46:69–79. https://doi.org/10.1016/j.compositesa.2012.07.019.
[15] Yang Z, Zhao B, Qin S, Hu Z, Jin Z, Wang J. Study on the mechanical properties of hybrid reinforced rigid polyurethane composite foam. J Appl Polym Sci 2004;92:1493–500. https://doi.org/10.1002/app.20071.
[16] Yao R, Pang T, He S, Li Q, Zhang B, Sun G. A bio-inspired foam-filled multi-cell structural configuration for energy absorption. Compos B Eng 2022;238:109801. https://doi.org/10.1016/j.compositesb.2022.109801.
[17] Zhang Z, Zhang Q, Zhang D, Li Y, Jin F, Fang D. Enhanced mechanical performance of brazed sandwich panels with high density square honeycomb-corrugation hybrid cores. Thin-Walled Struct 2020;151:106757. https://doi.org/10.1016/j.tws.2020.106757.
[18] Wang P, Yang F, Lu G, Bian Y, Zhang S, Zheng B, et al. Anisotropic compression behaviors of bio-inspired modified body-centered cubic lattices validated by additive manufacturing. Compos B Eng 2022;234:109724. https://doi.org/10.1016/j.compositesb.2022.109724.
[19] Côté F, Deshpande VS, Fleck NA, Evans AG. The compressive and shear responses of corrugated and diamond lattice materials. Int J Solid Struct 2006;43:6220–42. https://doi.org/10.1016/j.ijsolstr.2005.07.045.
[20] Cao X, Ji B, Li Y, An X, Fan H, Ke L. Multi-failure analyses of additively manufactured lattice truss sandwich cylinders. Compos B Eng 2021;207:108561. https://doi.org/10.1016/j.compositesb.2020.108561.
[21] Le VT, Ha NS, Goo NS. Advanced sandwich structures for thermal protection systems in hypersonic vehicles: a review. Compos B Eng 2021;226:109301. https://doi.org/10.1016/j.compositesb.2021.109301.
[22] Rubino V, Deshpande VS, Fleck NA. The dynamic response of end-clamped sandwich beams with a Y-frame or corrugated core. Int J Impact Eng 2008;35:829–44. https://doi.org/10.1016/j.ijimpeng.2007.10.006.
[23] Han B, Wang W, Zhang Z, Zhang Q, Jin F, Lu T. Performance enhancement of sandwich panels with honeycomb-corrugation hybrid core. Theor Appl Mech Lett 2016;6:54–9. https://doi.org/10.1016/j.taml.2016.01.001.
[24] Zhang Z, Han B, Zhang Q, Jin F. Free vibration analysis of sandwich beams with honeycomb-corrugation hybrid cores. Compos Struct 2017;171:335–44. https://doi.org/10.1016/j.compstruct.2017.03.045.
[25] Côté F, Deshpande VS, Fleck NA, Evans AG. The out-of-plane compressive behavior of metallic honeycombs. Mater Sci Eng, A 2004;380:272–80. https://doi.org/10.1016/j.msea.2004.03.051.
[26] Cote F, Deshpande V, Fleck N. The shear response of metallic square honeycombs. J Mech Mater Struct 2006;1:1281–99. https://doi.org/10.2140/jomms.2006.1.1281.
[27] Feng L-J, Wu L-Z, Yu G-C. An Hourglass truss lattice structure and its mechanical performances. Mater Des 2016;99:581–91. https://doi.org/10.1016/j.matdes.2016.03.100.
[28] Queheillalt DT, Wadley HNG. Pyramidal lattice truss structures with hollow trusses. Mater Sci Eng, A 2005;397:132–7. https://doi.org/10.1016/j.msea.2005.02.048.
[29] Rathbun HJ, Wei Z, He MY, Zok FW, Evans AG, Sypeck DJ, et al. Measurement and simulation of the performance of a lightweight metallic sandwich structure with a tetrahedral truss core. J Appl Mech 2004;71:368–74. https://doi.org/10.1115/1.1757487.
[30] Queheillalt DT, Wadley HNG. Hollow pyramidal lattice truss structures. Int J Mater Res 2011;102:389–400. https://doi.org/10.3139/146.110489.
[31] Zhang Q, Lu T. Experimental and simulated compressive properties of work-hardened X-type lattice truss structures. Acta Mech Solida Sin 2012;25:111–6. https://doi.org/10.1016/S0894-9166(12)60012-3.
[32] Zhang Q, Han Y, Chen C, Lu T. Ultralight X-type lattice sandwich structure (I): concept, fabrication and experimental characterization. Sci China Ser E Technol Sci 2009;52:2147–54. https://doi.org/10.1007/s11431-009-0219-9.
[33] Han B, Yu B, Xu Y, Chen C-Q, Zhang Q-C, Lu TJ. Foam filling radically enhances transverse shear response of corrugated sandwich plates. Mater Des 2015;77:132–41. https://doi.org/10.1016/j.matdes.2015.03.050.
[34] Gibson LJ. Mechanical behavior of metallic foams. Annu Rev Mater Sci 2000;30:191–227. https://doi.org/10.1146/annurev.matsci.30.1.191.
[35] Wang X-Z, Wu L-Z, Wang S-X. Tensile and shear properties of aluminium foam. Mater Technol 2009;24:161–5. https://doi.org/10.1179/106678509X12475884746705.
[36] Zhou Q, Mayer RR. Characterization of aluminum honeycomb material failure in large deformation compression, shear, and tearing. J Eng Mater Technol 2002;124:412–20. https://doi.org/10.1115/1.1491575.
[37] Zupan M, Chen C, Fleck NA. The plastic collapse and energy absorption capacity of egg-box panels. Int J Mech Sci 2003;45:851–71. https://doi.org/10.1016/S0020-7403(03)00136-X.
[38] Kooistra GW, Wadley HNG. Lattice truss structures from expanded metal sheet. Mater Des 2007;28:507–14. https://doi.org/10.1016/j.matdes.2005.08.013.
[39] Sugimura Y. Mechanical response of single-layer tetrahedral trusses under shear loading. Mech Mater 2004;36:715–21. https://doi.org/10.1016/j.mechmat.2003.05.002.
[40] Li Z, Chen W, Hao H. Crushing behaviours of folded kirigami structure with square dome shape. Int J Impact Eng 2018;115:94–105. https://doi.org/10.1016/j.ijimpeng.2018.01.013.
[41] Fischer S. Realistic Fe simulation of foldcore sandwich structures. Int J Mech Mater Eng 2015;10:14. https://doi.org/10.1186/s40712-015-0041-z.
[42] Zurnaci E, Gökkaya H. The effect of core configuration on the compressive performance of metallic sandwich panels. Mater Tehnol 2019;53:859–64. https://doi.org/10.17222/mit.2019.023.
[43] Zhang Y, Yan L, Zhang W, Su P, Han B, Guo S. Metallic tube-reinforced aluminum honeycombs: compressive and bending performances. Compos B Eng 2019;171:192–203. https://doi.org/10.1016/j.compositesb.2019.04.044.
[44] St-Pierre L, Fleck NA, Deshpande VS. Sandwich Beams with Corrugated and Y-frame cores: does the back face contribute to the bending response? J Appl Mech Trans ASME 2012;79:1–13. https://doi.org/10.1115/1.4004555.
[45] Dong L, Deshpande V, Wadley H. Mechanical response of Ti–6Al–4V octet-truss lattice structures. Int J Solid Struct 2015;60(61):107–24. https://doi.org/10.1016/j.ijsolstr.2015.02.020.
[46] Dong L. Mechanical response of Ti–6Al–4V hierarchical architected metamaterials. Acta Mater 2019;175:90–106. https://doi.org/10.1016/j.actamat.2019.06.004.
[47] Radford DD, Deshpande VS, Fleck NA. The use of metal foam projectiles to simulate shock loading on a structure. Int J Impact Eng 2005;31:1152–71. https://doi.org/10.1016/j.ijimpeng.2004.07.012.
[48] Menkes SB, Opat HJ. Broken beams - tearing and shear failures in explosively loaded clamped beams. Exp Mech 1973;13:480–6. https://doi.org/10.1007/BF02322734.
[49] McShane GJ, Pingle SM, Deshpande VS, Fleck NA. Dynamic buckling of an inclined strut. Int J Solid Struct 2012;49:2830–8. https://doi.org/10.1016/j.ijsolstr.2012.03.045.
[50] Stout MG, Follansbee PS. Strain rate sensitivity, strain hardening, and yield behavior of 304L stainless steel. J Eng Mater Technol 1986;108:344–53. https://doi.org/10.1115/1.3225893.
[51] Sun G, Chen D, Wang H, Hazell PJ, Li Q. High-velocity impact behaviour of aluminium honeycomb sandwich panels with different structural configurations. Int J Impact Eng 2018;122:119–36. https://doi.org/10.1016/j.ijimpeng.2018.08.007.
[52] Deshpande VS, Fleck NA. Isotropic constitutive models for metallic foams. J Mech Phys Solid 2000;48:1253–83. https://doi.org/10.1016/S0022-5096(99)00082-4.
[53] Xiang X, Zou S, Ha NS, Lu G, Kong I. Energy absorption of bio-inspired multi-layered graded foam-filled structures under axial crushing. Compos B Eng 2020;198:108216. https://doi.org/10.1016/j.compositesb.2020.108216.
[54] Deshpande VS, Fleck NA. High strain rate compressive behaviour of aluminium alloy foams. Int J Impact Eng 2000;24:277–98. https://doi.org/10.1016/S0734-743X(99)00153-0.
[55] Uth T, Deshpande VS. Response of clamped sandwich beams subjected to high-velocity impact by sand slugs. Int J Impact Eng 2014;69:165–81. https://doi.org/10.1016/j.ijimpeng.2014.02.012.
[56] Qin Q, Yuan C, Zhang J, Wang TJ. A simplified analytical model for metal sandwich beam with soft core under impulsive loading over a central patch. Int J Impact Eng 2014;74:67–82. https://doi.org/10.1016/j.ijimpeng.2014.06.008.
[57] Jing L, Wang Z, Ning J, Zhao L. The dynamic response of sandwich beams with open-cell metal foam cores. Compos B Eng 2011;42:1–10. https://doi.org/10.1016/j.compositesb.2010.09.024.
[58] Li S, Guo X, Liao J, Li Q, Sun G. Crushing analysis and design optimization for foam-filled aluminum/CFRP hybrid tube against transverse impact. Compos B Eng 2020;196:108029. https://doi.org/10.1016/j.compositesb.2020.108029.
[59] Hanssen AG, Hopperstad OS, Langseth M, Ilstad H. Validation of constitutive models applicable to aluminium foams. Int J Mech Sci 2002;44:359–406. https://doi.org/10.1016/S0020-7403(01)00091-1.
[60] Gibson LJ, Ashby MF. Cellular solids, vol. 28. Cambridge University Press; 1997. https://doi.org/10.1017/CBO9781139878326.